ATLAS NOTE

ATLAS-CONF-2016-037

4th August 2016

Search for supersymmetry with two same-sign leptons or three leptons using 13.2 fb^{-1} of $\sqrt{s}$ = 13 TeV pp collision data collected by the ATLAS detector

The ATLAS Collaboration

Abstract

This note presents a search for strongly produced supersymmetric particles using signatures involving multiple energetic jets and either two isolated same-sign leptons (e or μ) or at least three isolated leptons. The analysis also utilises other observables, such as b-tagged jets or missing transverse momentum, to extend its sensitivity. A data sample of proton–proton collisions at $\sqrt{s}$ = 13 TeV recorded with the ATLAS detector at the Large Hadron Collider in 2015 and 2016, corresponding to a total integrated luminosity of 13.2 fb^{-1}, is used for the search. No significant excess over the Standard Model expectation is observed. The results are interpreted in several simplified supersymmetric models featuring R-parity conservation and R-parity violation, extending the exclusion limits from previous searches.

ATLAS-CONF-2016-037
05 August 2016

© 2016 CERN for the benefit of the ATLAS Collaboration.
Reproduction of this article or parts of it is allowed as specified in the CC-BY-4.0 license.

1 Introduction

Supersymmetry (SUSY) [1–6] is one of the most studied frameworks to extend the Standard Model (SM) beyond the electroweak scale; a general review can be found in Ref. [7]. In its minimal realisation (the MSSM) [8, 9] it predicts a new bosonic (fermionic) partner for each fundamental SM fermion (boson), as well as an additional Higgs doublet. If R-parity is conserved [10] the lightest supersymmetric particle (LSP) is stable and is typically the lightest neutralino[1] $\tilde{\chi}_1^0$. In many models, the LSP can be a viable dark matter candidate [11, 12] and produce collider signatures with large missing transverse momentum.

In order to address the SM hierarchy problem with SUSY models [13–16], TeV-scale masses are required [17, 18] for the partners of the gluons (gluinos $\tilde{g}$) and of the top quark chiral degrees of freedom (top squarks $\tilde{t}_\mathrm{L}$ and $\tilde{t}_\mathrm{R}$), due to the large top Yukawa coupling[2]. The latter also favours significant $\tilde{t}_\mathrm{L}$–$\tilde{t}_\mathrm{R}$ mixing, so that the lighter mass eigenstate $\tilde{t}_1$ is in many scenarios lighter than the other squarks [19, 20]. Bottom squarks ($\tilde{b}$) may also be light, being bound to top squarks by $SU(2)_\mathrm{L}$ invariance. This leads to potentially large production cross-sections for gluino pairs ($\tilde{g}\tilde{g}$), top–antitop squark pairs ($\tilde{t}_1\tilde{t}_1^*$) and bottom–antibottom squark pairs ($\tilde{b}_1\tilde{b}_1^*$) at the Large Hadron Collider (LHC) [21]. Production of isolated leptons may arise in the cascade decays of those superpartners to SM quarks and neutralinos $\tilde{\chi}_1^0$, via intermediate neutralinos $\tilde{\chi}_{2,3,4}^0$ or charginos $\tilde{\chi}_{1,2}^\pm$ that in turn lead to W, Z or Higgs bosons, or to lepton superpartners (sleptons). Lighter third-generation squarks would also enhance $\tilde{g} \to t\tilde{t}_1^*$ or $\tilde{g} \to b\tilde{b}_1^*$ branching ratios over the generic decays involving light-flavour squarks, favouring the production of heavy flavour quarks and, in the case of top quarks, additional leptons.

This note presents a search for SUSY in final states with two leptons (electrons or muons) of the same electric charge (referred to as same-sign (SS) leptons) or three leptons (3L) in any charge combination, jets and in some cases also missing transverse momentum (whose magnitude is referred to as $E_\mathrm{T}^\mathrm{miss}$). It is an extension of an earlier search performed by ATLAS with $\sqrt{s} = 13$ TeV data [22], and uses the data collected by the ATLAS experiment [23] in proton–proton (pp) collisions during 2015 and 2016. A similar search for SUSY in this topology was also performed by the CMS Collaboration at $\sqrt{s} = 13$ TeV [24]. While the same-sign leptons signature is present in many scenarios of physics beyond the SM (BSM), SM processes leading to such final states have very small cross-sections. Compared to other BSM searches, analyses based on same-sign leptons therefore allow the use of looser kinematic requirements (for example, on $E_\mathrm{T}^\mathrm{miss}$ or the momentum of jets and leptons), preserving sensitivity to scenarios with small mass differences between gluinos/squarks and the LSP, or in which R-parity is not conserved.

The sensitivity to a wide range of models is illustrated by the interpretation of the results in the context of four different R-parity conserving (RPC) and four R-parity violating (RPV) SUSY benchmark processes that may lead to same-sign or three-lepton signatures. For RPC models, the first two scenarios focus on gluino pair production with generic decays into light quarks and multiple leptons, either involving light sleptons and sneutrinos, $\tilde{g} \to q\bar{q}\tilde{\chi}_2^0 \to q\bar{q}(\ell\tilde{\ell}^*/\nu\tilde{\nu}^*) \to q\bar{q}(\ell^+\ell^-/\nu\nu)\tilde{\chi}_1^0$ (shown in Fig. 1(a)), or mediated by a cascade involving a $\tilde{\chi}_1^\pm$ and a $\tilde{\chi}_2^0$, $\tilde{g} \to q\bar{q}'\tilde{\chi}_1^\pm \to q\bar{q}'W^\pm\tilde{\chi}_2^0 \to q\bar{q}'W^\pm Z\tilde{\chi}_1^0$ (shown in Fig. 1(b)). The other two RPC scenarios are motivated by the expectation that the third-generation squarks are lighter than the other squarks and target the direct production of $\tilde{b}_1\tilde{b}_1^*$ pairs with subsequent chargino-mediated

---

[1] The SUSY partners of the Higgs and electroweak gauge bosons mix to form the mass eigenstates known as charginos ($\tilde{\chi}_l^\pm$, $l = 1, 2$ ordered by increasing mass) and neutralinos ($\tilde{\chi}_m^0$, $m = 1, \ldots, 4$ ordered by increasing mass).

[2] The partners of the left-handed (right-handed) quarks are labelled $\tilde{q}_{L(R)}$. In the case where there is significant L/R mixing (as is the case for third generation squarks) the mass eigenstates of these squarks are labelled $\tilde{q}_{1,2}$ ordered in increasing mass.

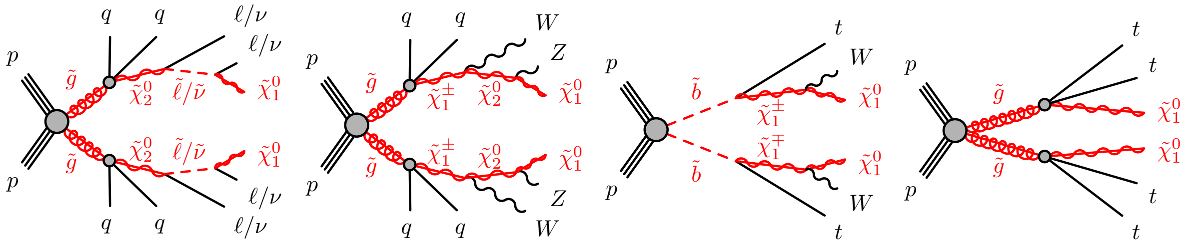

(a) (b) (c) (d)

Figure 1: RPC SUSY processes featuring gluino (a, b, d) or bottom squark (c) pair production considered in this analysis.

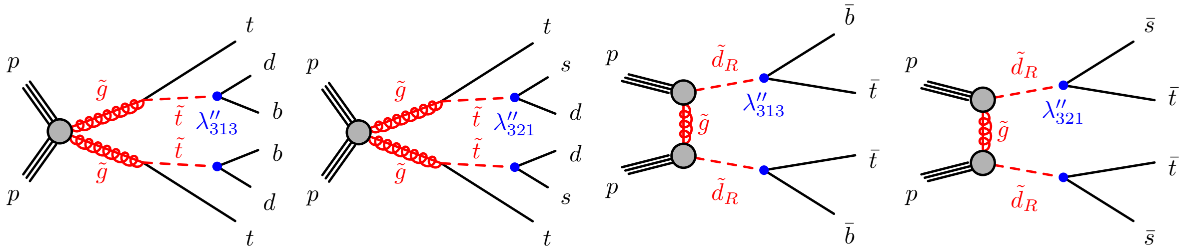

(a) (b) (c) (d)

Figure 2: RPV SUSY processes featuring gluino (a,b) or right-handed down squark (c,d) pair production and decays via baryon number-violating couplings λ'' considered in this analysis.

$\tilde{b}_1 \to tW^- \tilde{\chi}_1^0$ decays (shown in Fig. 1(c)) or the production of $\tilde{g}\tilde{g}$ pairs decaying as $\tilde{g} \to t\bar{t}\tilde{\chi}_1^0$ via an off-shell top squark (shown in Fig. 1(d)).

In the case of non-zero RPV couplings in the baryonic sector ($\lambda''_{ijk} \neq 0$), as proposed in Minimal Flavor Violation scenarios [25–27], gluino and squarks may decay directly to top quarks, leading to final states with same-sign leptons [28, 29] and b-tagged jets. Due to the absence of neutralinos in the final state, lower $E_{\mathrm{T}}^{\mathrm{miss}}$ is expected in these scenarios since it can only arise from the neutrinos produced in the top quark decays. Benchmark scenarios with gluino pair production followed by top-squark-mediated decay (shown in Figs. 2(a), 2(b)), or with pair-production of right-handed[3] like-sign down squarks (shown in Figs. 2(c), 2(d)) are considered in this note.

In all these scenarios, antisquarks decay into the charge-conjugate final states of those indicated for the corresponding squarks, and gluinos decay with equal probabilities into a certain final state or its charge conjugate.

Different signal regions (SRs) are designed to achieve good sensitivity for these RPC and RPV SUSY scenarios, mainly characterised by the number of b-tagged jets or reconstructed leptons. They are detailed in Section 4, preceded by descriptions of the experimental apparatus (Section 2) and the simulated event samples (Section 3). Section 5 describes to the estimation of the contribution from SM processes to the signal regions, validated by comparisons with data in dedicated regions. The results are presented in Section 6 together with the statistical procedure used to interpret the results in the context of the SUSY benchmark scenarios. Finally, Section 7 summarises the main conclusions of this note.

---

[3] These RPV baryon-number-violating couplings only couple to $SU(2)$ singlets.

2 The ATLAS detector

The ATLAS experiment [23] is a multi-purpose particle detector with a forward-backward symmetric cylindrical geometry and nearly 4π coverage in solid angle.[4] The interaction point is surrounded by an inner detector (ID), a calorimeter system, and a muon spectrometer (MS).

The ID provides precision tracking of charged particles for pseudorapidities $|\eta| < 2.5$ and is surrounded by a superconducting solenoid providing a 2 T axial magnetic field. It consists of pixel and silicon-microstrip detectors inside a transition radiation tracker.

In the pseudorapidity region $|\eta| < 2.5$, high-granularity lead/liquid-argon electromagnetic sampling calorimeters are used. A steel/scintillator tile calorimeter measures hadron energies for $|\eta| < 1.7$. The endcap and forward regions, spanning $1.5 < |\eta| < 4.9$, are instrumented with liquid-argon calorimeters for both the electromagnetic and hadronic measurements.

The MS consists of three large superconducting toroids with eight coils each, a system of trigger and precision-tracking chambers, which provide triggering and tracking capabilities in the ranges $|\eta| < 2.4$ and $|\eta| < 2.7$, respectively.

A two-level trigger system is used to select events [30]. The first-level trigger is implemented in hardware. This is followed by the software-based High-Level Trigger stage, which can run offline-like reconstruction and calibration software, reducing the event rate to about 1 kHz.

3 Dataset and simulated event samples

The data were collected by the ATLAS detector during 2015 with a peak instantaneous luminosity of $L = 5.2 \times 10^{33}$ cm^{-2}s^{-1}, and up to July 2016 with a peak instantaneous luminosity of $L = 1.1 \times 10^{34}$ cm^{-2}s^{-1}, with a mean number of pp interactions per bunch crossing (pile-up) in the dataset of $\langle\mu\rangle = 14$ in 2015 and $\langle\mu\rangle = 22$ in 2016. After the application of beam, detector and data quality requirements, the integrated luminosity considered in this analysis corresponds to 13.2 fb^{-1}. The preliminary uncertainty on the combined 2015+2016 integrated luminosity is 2.9%. It is derived, following a methodology similar to that detailed in Refs. [31] and [32], from a preliminary calibration of the luminosity scale using x-y beam-separation scans performed in August 2015 and May 2016.

Monte Carlo (MC) simulated event samples are used to estimate the background from SM processes and to model the SUSY signals. The MC samples are processed through an ATLAS detector simulation [33] based on GEANT4 [34] or a fast simulation using a parameterisation of the calorimeter response and GEANT4 for the ID and MS [35], and are reconstructed in the same manner as the data.

Diboson processes with four charged leptons (ℓ), three charged leptons and one neutrino, or two charged leptons and two neutrinos are simulated using the SHERPA v2.1.1 generator [36], and are described in detail in Ref. [37]. The matrix elements contain the doubly resonant WW, WZ and ZZ processes and all other

---

[4] ATLAS uses a right-handed coordinate system with its origin at the nominal interaction point (IP) in the centre of the detector and the z-axis along the beam pipe. The x-axis points from the IP to the centre of the LHC ring, and the y-axis points upward. Cylindrical coordinates (r, ϕ) are used in the transverse plane, ϕ being the azimuthal angle around the beam pipe. The pseudorapidity is defined in terms of the polar angle θ as $\eta = -\ln\tan(\theta/2)$. Rapidity is defined as $y = 0.5\ln\left[(E + p_z)/(E - p_z)\right]$ where E denotes the energy and p_z is the component of the momentum along the beam direction.

diagrams with four or six electroweak vertices (such as same-sign W boson production in association with two jets, $W^{\pm}W^{\pm}jj$). Fully leptonic triboson processes (WWW, WWZ, WZZ and ZZZ) with up to six charged leptons are also simulated using Sherpa v2.1.1 and described in Ref. [37]. The 4ℓ and $2\ell + 2\nu$ processes are calculated at next-to-leading order (NLO) for up to one additional parton; final states with two and three additional partons are calculated at leading order (LO). The $WWZ \rightarrow 4\ell + 2\nu$ or $2\ell + 4\nu$ processes are calculated at LO with up to two additional partons. The $3\ell + 1\nu$ process is calculated at NLO and up to three extra partons at LO using the Comix [38] and OpenLoops [39] matrix element generators and merged with the Sherpa parton shower [40] using the ME+PS@NLO prescription [41]. The $WWZ/WZZ \rightarrow 3\ell + 3\nu$, $ZZZ \rightarrow 6\ell + 0\nu$, $4\ell + 2\nu$ or $2\ell + 4\nu$ processes are calculated with the same configuration but with up to only two extra partons at LO. The CT10 [42] parton distribution function (PDF) set is used for all Sherpa samples in conjunction with a dedicated tuning of the parton shower parameters developed by the Sherpa authors. The generator cross-sections (at NLO for most of the processes) are used when normalising these backgrounds.

Samples of $t\bar{t}V$ (with $V = W$ and Z, including non-resonant Z/γ^{*} contributions) and $t\bar{t}WW$ production are generated at LO with MadGraph5_aMC@NLO v2.2.2 [43] interfaced to the Pythia 8.186 [44] parton shower model, with up to two ($t\bar{t}W$), one ($t\bar{t}Z$) or no ($t\bar{t}WW$) extra partons included in the matrix element; they are described in detail in [45]. MadGraph5_aMC@NLO is also used to simulate the tZ, tWZ, $t\bar{t}t\bar{t}$ and $t\bar{t}t$ processes. The A14 set of tuned parameters (tune) [46] is used together with the NNPDF23LO PDF set [47]. The $t\bar{t}W$, $t\bar{t}Z$, $t\bar{t}WW$ and $t\bar{t}t\bar{t}$ events are normalised to their NLO cross-section [43] while the generator cross-section is used for tZ, $t\bar{t}t$ and tWZ.

Production of a Higgs boson in association with a $t\bar{t}$ pair is simulated using MadGraph5_aMC@NLO interfaced to Herwig 2.7.1 [48]. The UEEE5 underlying-event tune is used together with the CTEQ6L1 [49] (matrix element) and CT10 (parton shower) PDF sets. Simulated samples of SM Higgs boson production in association with a W or Z boson are produced with Pythia 8.186, using the A14 tune and the NNPDF23LO PDF set. Events are normalised with cross-sections calculated at NLO [50].

The RPC SUSY signal processes are generated from LO matrix elements with up to two extra partons (only up to one for the $\tilde{g} \rightarrow q\bar{q}(\ell\ell/\nu\nu)\tilde{\chi}_1^0$ model), using the MadGraph5_aMC@NLO v2.2.3 generator interfaced to Pythia 8.186 with the A14 tune for the modelling of the SUSY decay chain, parton showering, hadronisation and the description of the underlying event. For the RPV SUSY models, the MadGraph5_aMC@NLO v2.3.3 generator interfaced to Pythia 8.210 are used instead. Parton luminosities are provided by the NNPDF23LO PDF set. Jet–parton matching is realised following the CKKW-L prescription [51], with a matching scale set to one quarter of the pair-produced superpartner mass. All signal models are generated with prompt decays of the SUSY particles. Signal cross-sections are generally calculated to NLO in the strong coupling constant, adding the resummation of soft gluon emission at next-to-leading-logarithmic accuracy (NLO+NLL) [52–56]. The nominal cross-section and the uncertainty are taken from an envelope of cross-section predictions using different PDF sets and factorisation and renormalisation scales, as described in Ref. [57]; the NLO+NLL cross-section being used for gluinos and bottom squarks production, while only NLO cross-sections are available for like-sign down squark pair production [52, 58].

In all MC samples, except those produced by Sherpa, the EvtGen v1.2.0 program [59] is used to model the properties of the bottom and charm hadron decays. To simulate the effects of additional pp collisions in the same and nearby bunch crossings, additional interactions are generated using the soft QCD processes of Pythia 8.186 with the A2 tune [60] and the MSTW2008LO PDF [61], and overlaid onto the simulated hard scatter event. The Monte Carlo samples are reweighted to match the pile-up conditions observed in the data.

4 Event selection

Candidate events are required to have a reconstructed vertex [62], with at least two associated tracks with $p_{\mathrm{T}} > 400$ MeV, and the vertex with the highest sum of squared transverse momentum of the tracks is considered as the primary vertex. In order to perform background estimations using data, two categories of electrons and muons are defined: "candidate" and "signal" (the latter being a subset of the "candidate" leptons satisfying tighter selection criteria).

Electron candidates are reconstructed from energy depositions in the electromagnetic calorimeter that have been matched to an ID track and are required to have $|\eta| < 2.47$, a transverse momentum $p_{\mathrm{T}} > 10$ GeV, and to pass a loose likelihood-based identification requirement [63]. The likelihood input variables include measurements of calorimeter shower shapes and track properties from the ID. Candidates within the transition region between the barrel and endcap electromagnetic calorimeters, $1.37 < |\eta| < 1.52$, are removed. The track matched with the electron must have a significance of the transverse impact parameter with respect to the reconstructed primary vertex, d_0, of $|d_0|/\sigma(d_0) < 5$.

Muon candidates are reconstructed in the region $|\eta| < 2.5$ from muon spectrometer tracks matching ID tracks. All muon candidates must have $p_{\mathrm{T}} > 10$ GeV and must pass the medium identification requirements defined in Ref. [64], based on selections on the number of hits in the different ID and muon spectrometer subsystems, and the significance of the charge-to-momentum ratio q/p [64].

Jets are reconstructed with the anti-k_t algorithm [65] with radius parameter $R = 0.4$, using three-dimensional topological energy clusters in the calorimeter [66] as input. All jets must have $p_{\mathrm{T}} > 20$ GeV and $|\eta| < 2.8$. Jets are calibrated as described in Ref. [67]. In order to reduce the effects of pile-up, for jets with $p_{\mathrm{T}} < 60$ GeV and $|\eta| < 2.4$ a significant fraction of the tracks associated with each jet must have an origin compatible with the primary vertex, as defined by the jet vertex tagger [68]. Furthermore, for all jets the expected average energy contribution from pile-up clusters is subtracted according to the jet area [67].

Identification of jets containing b-hadrons (b-tagging) is performed with the MV2c10 algorithm, a multivariate discriminant making use of track impact parameters and reconstructed secondary vertices [69, 70]. A requirement is chosen corresponding to a 70% average efficiency for tagging b-jets in simulated $t\bar{t}$ events. The rejection factors for light-quark/gluon jets, c-quark jets and hadronically decaying τ leptons in simulated $t\bar{t}$ events are approximately 380, 12 and 54, respectively [70, 71]. Jets with $|\eta| < 2.5$ which satisfy this b-tagging requirement are identified as b-jets. To compensate for differences between data and MC simulation in the b-tagging efficiencies and mis-tagging rates, correction factors are applied to the simulated samples [70].

After object identification, overlaps between the different objects are resolved. Any jet within a distance $\Delta R_y = \sqrt{(\Delta y)^2 + (\Delta\phi)^2} = 0.2$ of a lepton candidate is discarded, unless the jet has a value of the MV2c10 discriminant larger than the value corresponding to approximately 85% b-tagging efficiency, in which case the lepton is discarded since it is likely originating from a semileptonic b-hadron decay. Any remaining lepton within $\Delta R_y = \min\{0.4, 0.04 + 10\,\mathrm{GeV}/p_{\mathrm{T}}(\ell)\}$ of a non-pileup jet is discarded. However, if the jet has fewer than three associated tracks or the muon p_{T} has more than $0.5 p_{\mathrm{T}}^{\mathrm{jet}}$ and more than $0.7 \sum p_{\mathrm{T}}^{\mathrm{jet\ tracks}}$, where $\sum p_{\mathrm{T}}^{\mathrm{jet\ tracks}}$ is the sum of track p_{T} for the tracks inside the jet, the muon is retained and the jet is discarded instead to avoid inefficiencies for high-energy muons undergoing significant energy loss in the calorimeter. Any calo-tagged muon[5] sharing an ID track with an electron is removed. Finally, any electron sharing an ID track with the remaining muons is also removed.

Signal electrons must satisfy a medium likelihood-based identification requirement [63] and have $|\eta| < 2$ to reduce the impact of electron charge mis-identification. Signal muons must fulfil the requirement of $|d_0|/\sigma(d_0) < 3$. The track associated to the signal leptons must have a longitudinal impact parameter with respect to the reconstructed primary vertex, z_0, satisfying $|z_0 \sin\theta| < 0.5$ mm. Isolation requirements are applied to both the signal electrons and muons. The scalar sum of the p_{T} of tracks within a variable-size cone around the lepton, excluding its own track, must be less than 6% of the lepton p_{T}. The track isolation cone radius for electrons (muons) $\Delta R_\eta = \sqrt{(\Delta\eta)^2 + (\Delta\phi)^2}$ is given by the smaller of $\Delta R_\eta = 10\ \mathrm{GeV}/p_{\mathrm{T}}$ and $\Delta R_\eta = 0.2\,(0.3)$, that is, a cone of size 0.2 (0.3) at low p_{T} but narrower for high-p_{T} leptons. In addition, in the case of electrons the energy of calorimeter energy clusters in a cone of $\Delta R_\eta = 0.2$ around the electron (excluding the deposition from the electron itself) must be less than 6% of the electron p_{T}. Simulated events are corrected to account for minor differences in the lepton trigger, reconstruction, identification and isolation efficiencies between data and MC simulation.

The missing transverse momentum (and its magnitude $E_{\mathrm{T}}^{\mathrm{miss}}$) is defined as the negative vector sum of the transverse momenta of all identified physics objects (electrons, photons [72], muons, jets) and an additional soft term. The soft term is constructed from all tracks that are not associated with any physics object, and that are associated with the primary vertex. In this way, the $E_{\mathrm{T}}^{\mathrm{miss}}$ is adjusted for the best calibration of the jets and the other identified physics objects above, while maintaining pile-up independence in the soft term [73, 74].

Events are selected using a combination (logical OR) of dilepton and $E_{\mathrm{T}}^{\mathrm{miss}}$ triggers, the latter being used only for events with $E_{\mathrm{T}}^{\mathrm{miss}} > 250\,\mathrm{GeV}$. The trigger-level requirements on $E_{\mathrm{T}}^{\mathrm{miss}}$ and the leading and subleading lepton p_{T} are looser than those applied offline to ensure that trigger efficiencies are constant in the relevant phase space. Events of interest are selected if they contain at least two signal leptons with $p_{\mathrm{T}} > 20$ GeV. If the event contains exactly two signal leptons, they are required to have the same electric charge. Events are discarded if they contain any jet failing basic quality selection criteria that reject detector noise and non-collision backgrounds [75].

To maximise the sensitivity to different signal models, nine overlapping signal regions are defined as shown in Table 1, with requirements on the number of signal leptons ($N_{\mathrm{lept}}^{\mathrm{signal}}$), the number of b-jets with $p_{\mathrm{T}} > 20\,\mathrm{GeV}$ ($N_{b\mathrm{-jets}}^{20}$), the number of jets with different p_{T} thresholds (25, 40 or 50 GeV) regardless of their flavour (N_{jets}), $E_{\mathrm{T}}^{\mathrm{miss}}$, the effective mass ($m_{\mathrm{eff}}$), defined as the scalar sum of the p_{T} of the signal leptons and jets (regardless of their flavour) in the event plus the $E_{\mathrm{T}}^{\mathrm{miss}}$, and the charge of the leptons in the event.

Each signal region is motivated by a different SUSY scenario. The SR3L1-SR3L2 and SR0b1-SR0b2 signal regions are sensitive to squarks of the first and second generations directly produced or appearing in gluino decays in RPC models, leading to final states particularly rich in leptons (Fig. 1(a)) or in jets (Fig. 1(b)), but with no enhancement of the production of b-quarks. Third-generation squark RPC models resulting in final states with two b-quarks, such as direct bottom squark production (Fig. 1(c)), are targeted by the SR1b signal region. Finally, the signal region SR3b targets production of gluinos decaying via a top squark resulting in final states with four b-quarks (Fig. 1(d)).

---

[5] A calo-tagged muon is a muon identified solely by calorimeter based identification (so no signal in MS) and are relevant only at $|\eta| < 0.1$.

Table 1: Summary of the event selection criteria for the signal regions (see text for details).

Signal region	$N_{\text{lept}}^{\text{signal}}$	$N_{b\text{-jets}}^{20}$	N_{jets}	$p_{\text{T,jets}}$ [GeV]	$E_{\text{T}}^{\text{miss}}$ [GeV]	m_{eff} [GeV]	Other
SR3L1	≥ 3	$= 0$	≥ 4	40	> 150	-	-
SR3L2	≥ 3	$= 0$	≥ 4	40	> 200	> 1500	-
SR0b1	≥ 2	$= 0$	≥ 6	25	> 150	> 500	-
SR0b2	≥ 2	$= 0$	≥ 6	40	> 150	> 900	-
SR1b	≥ 2	≥ 1	≥ 6	25	> 200	> 650	-
SR3b	≥ 2	≥ 3	≥ 6	25	> 150	> 600	-
SR1b-DD	≥ 2	≥ 1	≥ 4	50	-	> 1200	≥ 2 negatively-charged leptons
SR3b-DD	≥ 2	≥ 3	≥ 4	50	-	> 1000	≥ 2 negatively-charged leptons
SR1b-GG	≥ 2	≥ 1	≥ 6	50	-	> 1800	-

Signal regions targeting RPV models contain no $E_{\text{T}}^{\text{miss}}$ requirement. The SR1b-DD and SR3b-DD signal regions are sensitive to direct down squark production with a λ''_{321} (Fig. 2(d)) and λ''_{313} (Fig. 2(c)) coupling, respectively. Models featuring gluino production decaying via top squark including a λ''_{313} (Fig. 2(a)) or λ''_{321} (Fig. 2(b)) coupling are explored with the SR1b-GG signal region.

The values of acceptance times efficiency of the SR selections for the SUSY signal models in Figs. 1-2 typically range between 1-8% for models with a light $\tilde{\chi}_1^0$ and 0.5-1.5% for models with a heavy $\tilde{\chi}_1^0$.

5 Background estimation

Two main sources of SM background can be distinguished in this analysis. The first category consists of events with two same-sign prompt leptons or at least three prompt leptons, mainly from $t\bar{t}V$ and diboson processes. The second category is the reducible background which includes events containing electrons with mis-measured charge, mainly from the production of top quark pairs, and events containing at least one non-prompt or fake lepton, which mainly originate from hadron decays in events containing top quarks or W bosons produced in association with jets.

5.1 Background estimation methods

The estimation of the SM background processes with two same-sign prompt leptons or at least three prompt leptons is performed using the MC samples described in Section 3. Since diboson and $t\bar{t}V$ events are the main backgrounds in the signal regions, dedicated validation regions with an enhanced contribution from these processes are defined to verify the background predictions (see Section 5.3).

Background events due to charge mis-identification, dominated by electrons having emitted a hard bremsstrahlung photon which subsequently converted to an electron–positron pair, are referred to as “charge-flip”. The probability of mis-identifying the charge of a muon is checked in both data and MC simulation, and found to be negligible in the kinematic range relevant to this analysis. The contribution of charge-flip events is estimated using the data. The electron charge-flip probability is extracted in a $Z/\gamma^* \to ee$ data sample using a likelihood fit which takes as input the numbers of same-sign and opposite-sign electron pairs observed in the sample. The charge-flip probability is a free parameter of the fit and is extracted as a function of the electron p_{T} and η. The event yield of this background in the signal or validation regions is obtained by applying the measured charge-flip probability to data regions with the same kinematic requirements as the signal or validation regions but with opposite-sign lepton pairs.

The contribution from fake or non-prompt (FNP) leptons (such as hadrons mis-identified as leptons, leptons originating from heavy-flavour decays, and electrons from photon conversions) is also estimated from the data with a matrix method similar to that described in Ref. [22]. In this method, two types of lepton identification criteria are defined: "tight", corresponding to the signal lepton criteria described in Section 4, and "loose", corresponding to candidate leptons after overlap removal. The matrix method relates the number of events containing prompt or FNP leptons to the number of observed events with tight or loose-not-tight leptons using the probability for loose prompt or FNP leptons to satisfy the tight criteria. The probability for loose prompt leptons to satisfy the tight selection criteria is obtained using a $Z/\gamma^* \rightarrow \ell\ell$ data sample and is modelled as a function of the lepton p_{T} and η. The probability for loose FNP leptons to satisfy the tight selection criteria is determined from data in a SS control region enriched in non-prompt leptons originating from heavy-flavour decays, mostly in semileptonic $t\bar{t}$ events. This region contains events with at least one b-jet, one well-isolated "tag" muon, and an additional loose electron or muon on which the measurement is performed. The efficiencies are measured as function of p_{T} after subtracting the small contribution from prompt lepton processes.

The estimated FNP yields in the SRs are consistent with those predicted by two alternative methods: the first one relies on MC simulation of processes with FNP leptons or charge-flipped electrons ($t\bar{t}$, V+jets) [22, 76], corrected to match the observed data in dedicated control regions. The second method relies on data events with only one lepton, which are the processes leading to FNP leptons, to extrapolate from low-$E_{\mathrm{T}}^{\mathrm{miss}}$ control regions to the SRs.

5.2 Systematic uncertainties on the background estimation

The systematic uncertainties related to the same-sign prompt leptons background estimation arise from the accuracy of the theoretical and experimental modelling in the MC simulation. The primary sources of systematic uncertainties are related to the jet energy scale calibration, jet energy resolution, b-tagging efficiency, and MC modelling and theoretical cross-section uncertainties. The statistical uncertainty of the simulated event samples is also taken into account.

The cross-sections used to normalise the MC samples are varied according to the uncertainty in the cross-section calculation, that is, 13% for $t\bar{t}W$ and 12% $t\bar{t}Z$ production [43], and 6% for diboson production. Additional uncertainties are assigned to these backgrounds to account for the modelling of the kinematic distributions in the MC simulation. For $t\bar{t}W$ and $t\bar{t}Z$, the predictions from the MadGraph5_aMC@NLO and Sherpa generators are compared, and the renormalisation and factorisation scales used to generate these samples are varied, leading to a ~30% uncertainty for these processes after the SR selections. For dibosons, uncertainties are estimated by varying the renormalisation, factorisation and resummation scales, leading to a ~40–50% uncertainty for these processes after the SR selections. For triboson, $t\bar{t}h$, $t\bar{t}t\bar{t}$ and tZ production processes, which constitute small backgrounds in most of the signal regions, a 50% uncertainty on their total contribution is assumed.

Uncertainties in the FNP lepton background estimate are assigned due to the limited number of data events with loose and tight leptons. In addition, systematic uncertainties of 50–60% are assigned to the probabilities for loose FNP leptons to satisfy the tight signal criteria to account for potentially different FNP compositions (heavy flavour, light flavour or conversions) between the regions used to measure these

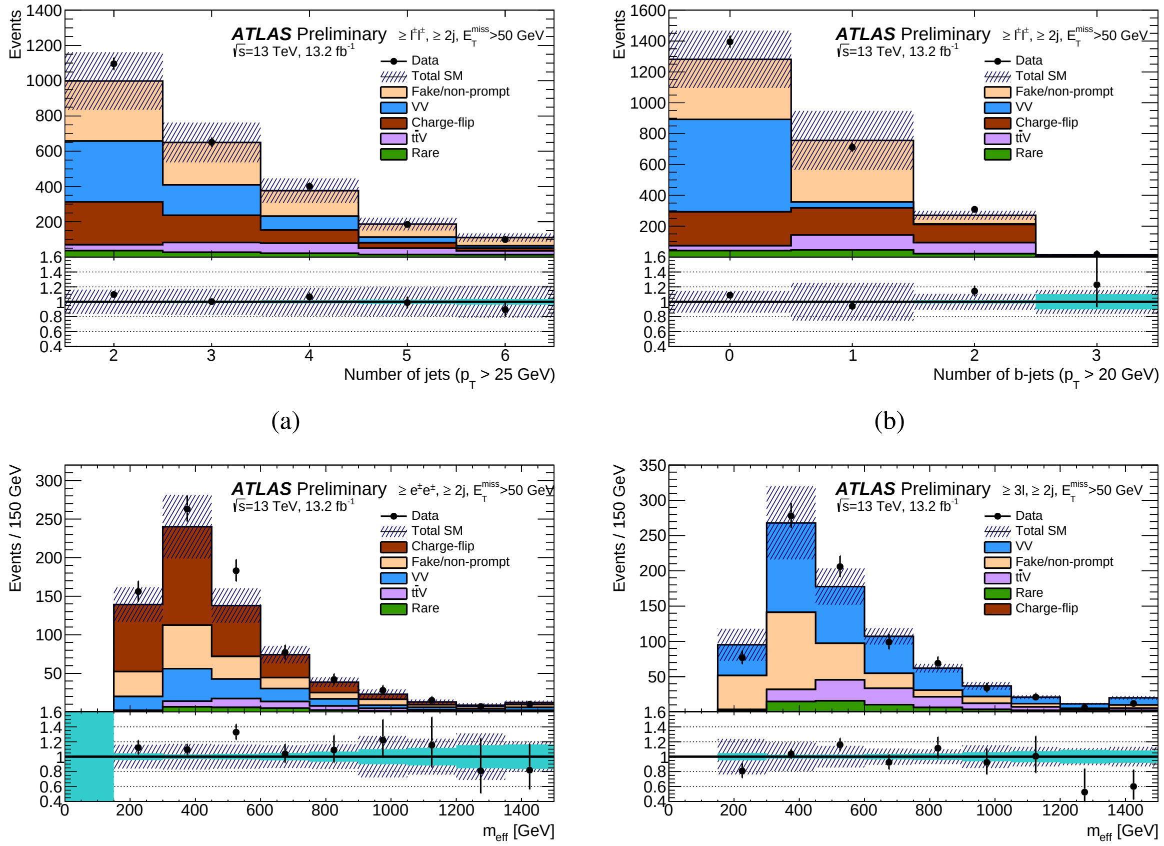

(a) (b)

(c) (d)

Figure 3: Distributions of the number of jets (a), of b-tagged jets (b) and the effective mass (c,d) after requiring at least two jets ($p_{\mathrm{T}} > 25$ GeV) and $E_{\mathrm{T}}^{\mathrm{miss}} > 50$ GeV, as well as at least two same-sign leptons (a,b) or two same-sign electrons (c) or three leptons (d). The statistical uncertainties in the background prediction are included in the uncertainty band, as well as the full systematic uncertainties for backgrounds with fake or non-prompt leptons, or charge-flip. The light-shaded bands in the ratio plots show contributions from statistical uncertainties alone. The "Rare" category contains the contributions from associated production of $t\bar{t}$ with $h/WW/t/t\bar{t}$, as well as tZ, tWZ, Wh, Zh, and triboson production.

probabilities and the SRs, as well as the contamination from prompt leptons in the former regions. This leads to overall FNP background uncertainties in the total background estimates of 5–32% depending on the signal region.

For the charge-flip background prediction, the main uncertainties originate from the statistical uncertainty of the charge-flip probability measurements and the background contamination of the sample used to extract the charge-flip probability.

5.3 Validation of background estimates

To check the validity and robustness of the background estimates, the distributions of several discriminating variables in data are compared with the predicted background after various requirements on the number of jets and b-jets. Examples of such distributions are shown in Fig. 3, and illustrate that the predictions

Table 2: Summary of the event selection in the validation regions (VRs). Requirements are placed on the number of signal leptons ($N^{\text{signal}}_{\text{lept}}$) and candidate leptons ($N^{\text{cand}}_{\text{lept}}$), the number of jets with $p_{\text{T}} > 25$ GeV (N^{25}_{jets}) or the number of b-jets with $p_{\text{T}} > 20$ GeV ($N^{20}_{b-\text{jets}}$), p_{T} of the lepton or jet, $E_{\text{T}}^{\text{miss}}$ and m_{eff}. The three leading-p_{T} leptons are referred to as $\ell_{1,2,3}$ with decreasing p_{T} and the two leading jets as $j_{1,2}$. In some validation regions, additional requirements are set on electron pseudorapidity, on the invariant mass of the two leading electrons m_{ee} or three leading leptons ($m_{\ell\ell\ell}$), the presence of SS leptons or a pair of same-flavour opposite-sign leptons (SFOS) and its invariant mass m_{SFOS}. In VR-$W^{\pm}W^{\pm}jj$, cuts on the transverse mass m_T (computed using the $E_{\text{T}}^{\text{miss}}$ and the highest-p_{T} lepton $m_{\text{T}}^2 = 2p_T^{\ell}E_{\text{T}}^{\text{miss}}(1 - \cos(\Delta\phi(\ell, E_{\text{T}}^{\text{miss}})))$ and the invariant mass of the two leading jets are added to increase the purity.

	$N^{\text{signal}}_{\text{lept}}$ ($N^{\text{cand}}_{\text{lept}}$)	$N^{20}_{b-\text{jets}}$	N^{25}_{jets}	$E_{\text{T}}^{\text{miss}}$ [GeV]	m_{eff} [GeV]	Other
VR-$W^{\pm}W^{\pm}jj$	= 2 (= 2) = 1 SS pair	= 0	≥ 2	> 50	> 500	$m(j_1j_2) > 500$ GeV $p_{\text{T}}(j_2) > 40$ GeV $p_{\text{T}}(\ell_2) > 25$ GeV $m_T > 40$ GeV veto $80 < m_{ee} < 100$ GeV
VR-WZ4j	= 3 (= 3)	= 0	≥ 4	> 20	> 300	$m_{\ell\ell\ell} > 100$ GeV
VR-$t\bar{t}W$	= 2 (-) = 1 SS pair	≥ 1	≥ 4 ($e^{\pm}\mu^{\pm}$) ≥ 3 ($\mu^{\pm}\mu^{\pm}$)	> 50	> 550	$p_{\text{T}}(\ell_2) > 30$ GeV veto $e^{\pm}e^{\pm}$ pairs
VR-$t\bar{t}Z$	≥ 3 (-) ≥ 1 SFOS pair	≥ 1	≥ 3	> 20	-	$p_{\text{T}}(\ell_2) > 25$ GeV $80 < m_{\text{SFOS}} < 100$ GeV
All VRs	Veto events belonging to any SR, or if ℓ_1 or ℓ_2 is an electron with $\lvert\eta\rvert > 1.37$ (except in VR-WZ4j and VR-$t\bar{t}Z$)					

Table 3: The numbers of observed data and expected background events for the validation regions. The "Rare" category contains the contributions from associated production of $t\bar{t}$ with $h/WW/t/t\bar{t}$, as well as tZ, tWZ, Wh, Zh, and triboson production. Background categories shown as "–" denote that they cannot contribute to a given region (e.g. charge flips in 3-lepton regions). The displayed yields include all sources of statistical and systematic uncertainties, except for the theoretical uncertainties which only consist of uncertainties on the inclusive production cross-sections.

	VR-WZ4j	VR-$W^{\pm}W^{\pm}jj$	VR-$t\bar{t}W$	VR-$t\bar{t}Z$
Observed	124	32	81	121
Total SM background	132 ± 26	26 ± 4	76 ± 19	139 ± 23
$t\bar{t}Z$	7.2 ± 1.6	0.19 ± 0.04	5.4 ± 0.9	66 ± 10
$t\bar{t}W$	0.59 ± 0.15	0.77 ± 0.18	17.3 ± 2.6	1.28 ± 0.21
$W^{\pm}W^{\pm}jj$	< 0.1	11.3 ± 0.9	0.83 ± 0.14	< 0.1
WZ	76 ± 16	5.2 ± 0.9	2.3 ± 0.6	18.1 ± 3.2
ZZ	10.6 ± 2.4	0.5 ± 0.4	0.07 ± 0.09	4.2 ± 1.4
Rare	4.8 ± 1.5	0.85 ± 0.29	8.6 ± 2.0	20 ± 10
Fake/non-prompt leptons	33 ± 18	5.8 ± 3.2	33 ± 19	29 ± 16
Charge-flip	–	1.37 ± 0.12	8.6 ± 0.6	–

and data agree fairly well. The background estimates in a kinematic region close to the signal regions can also be seen in Figs. 4 and 5, which show the $E_{\mathrm{T}}^{\mathrm{miss}}$ and m_{eff} distributions in the signal regions before applying the $E_{\mathrm{T}}^{\mathrm{miss}}$ or m_{eff} requirements.

Dedicated validation regions (VRs) are defined to test the estimate of the $t\bar{t}V$, WZ and $W^{\pm}W^{\pm}$ SM processes contributing to the signal regions. The corresponding selections are summarized in Table 2. In these regions, the overlap with the signal regions is resolved by vetoing events that contribute to the signal regions. To further reduce contributions from electron charge mis-identification, events are also vetoed in VR-$t\bar{t}W$ and VR-$W^{\pm}W^{\pm}jj$ if one of the two leading leptons is an electron with $|\eta| > 1.37$, since contributions from charge-flip electrons are smaller in the central region due to the lower amount of detector material in front of the calorimeters. The purity of the targeted processes in these regions ranges from about 20% to 50%.

The observed yields in these validation regions, compared with the background predictions and uncertainties, can be seen in Table 3. There is good agreement between data and the estimated background for the validation regions.

6 Results

Figures 4 and 5 show the $E_{\mathrm{T}}^{\mathrm{miss}}$ or m_{eff} distributions after the signal region selections (except that on the variable shown). The expected contributions from the SM backgrounds are also shown. The detailed yields for data and the different sources of SM background in the signal regions are presented in Tables 4 and 5. None of the observed events in data contain three leptons of equal charge. The uncertainties amount to 25–50% of the total background depending on the signal region. The contributions listed in the "Rare" category in the tables is dominated by tWZ and triboson production in SRs with 3 leptons, by $t\bar{t}H$ and tWZ production in SRs with a b-jet veto, by $t\bar{t}H$ and $t\bar{t}t\bar{t}$ production in SRs requiring one b-jet and by $t\bar{t}t\bar{t}$ production in SRs with three b-jets required.

In the absence of any significant deviations from the SM predictions, upper limits on possible BSM contributions to the signal regions are computed, using the SUSY benchmark scenarios described in Section 1. The HistFitter framework [77], which utilises a profile-likelihood-ratio test [78], is used to establish 95% confidence intervals using the $\mathrm{CL_s}$ prescription [79]. The likelihood is built as the product of a Poisson probability density function describing the observed number of events in the signal region and Gaussian distributions constraining the nuisance parameters associated with the systematic uncertainties whose widths correspond to the sizes of these uncertainties; Poisson distributions are used instead for MC and data control region statistical uncertainties.

Correlations of a given nuisance parameter between the different sources of backgrounds and the signal are taken into account when relevant. The hypothesis tests are performed independently for each of the signal regions.

Table 6 presents 95% confidence level (CL) model-independent upper limits on the number of BSM events, N_{BSM}, that may contribute to the signal regions. Normalising these by the integrated luminosity L of the data sample, they can be interpreted as upper limits on the visible BSM cross-section σ_{vis}, defined as the product $\sigma_{\mathrm{prod}} \times A \times \epsilon = N_{\mathrm{BSM}}/L$ of production cross-section (σ_{prod}), acceptance (A) and reconstruction efficiency (ϵ).

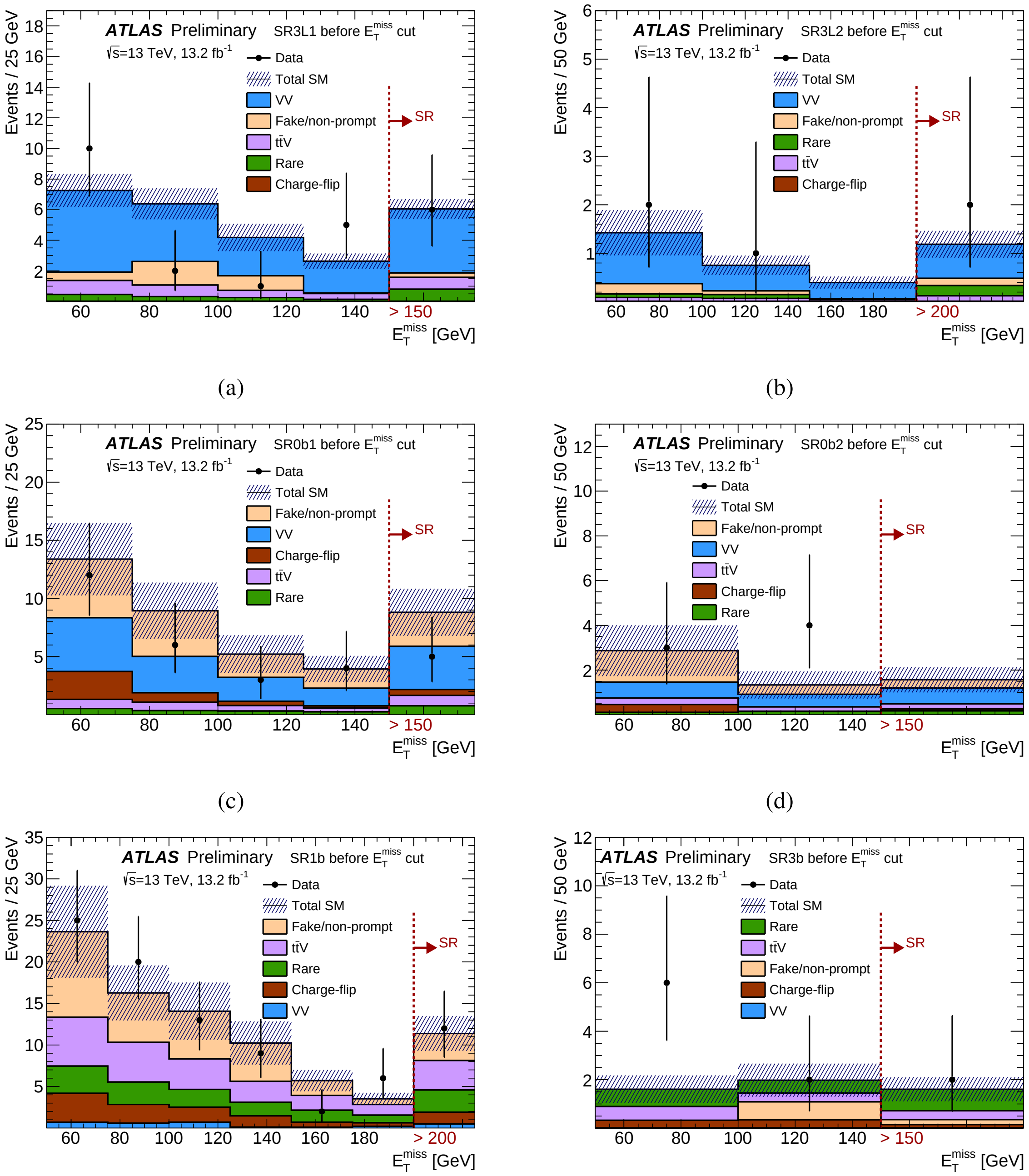

(a) (b)

(c) (d)

(e) (f)

Figure 4: Missing transverse momentum distributions after (a) SR3L1, (b) SR3L2, (c) SR0b1, (d) SR0b2, (e) SR1b and (f) SR3b selection, except the E_T^{miss} requirement. The results in the signal regions are shown in the last (inclusive) bin of each plot. The statistical uncertainties in the background prediction are included in the uncertainty band, as well as the full systematic uncertainties for backgrounds with fake or non-prompt leptons, or charge-flip. The "Rare" category contains the contributions from associated production of $t\bar{t}$ with $h/WW/t/t\bar{t}$, as well as tZ, tWZ, Wh, Zh, and triboson production.

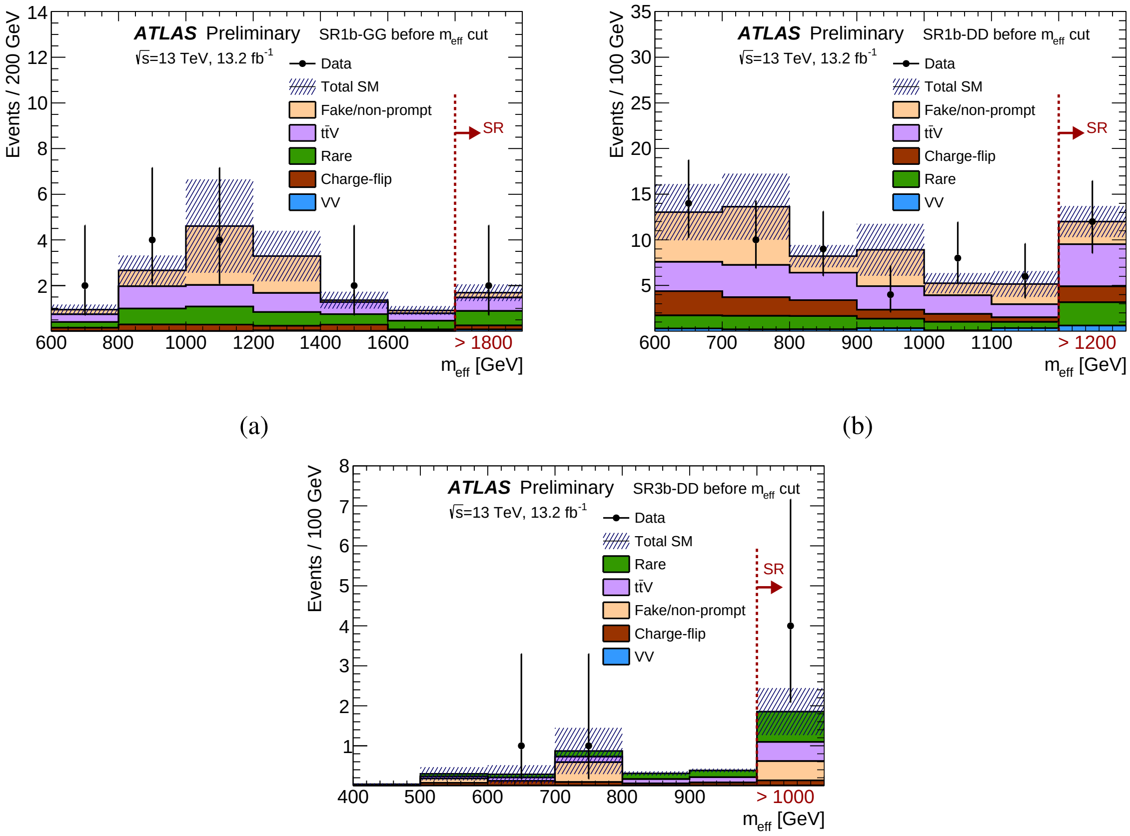

(a)

(b)

(c)

Figure 5: Effective mass distributions after (a) SR1b-GG, (b) SR1b-DD and (c) SR3b-DD selection, except the m_{eff} requirement. The results in the signal regions are shown in the last (inclusive) bin of each plot. The statistical uncertainties in the background prediction are included in the uncertainty band, as well as the full systematic uncertainties for backgrounds with fake or non-prompt leptons, or charge-flip. The "Rare" category contains the contributions from associated production of $t\bar{t}$ with $h/WW/t/t\bar{t}$, as well as tZ, tWZ, Wh, Zh, and triboson production.

Table 4: The number of observed data events and expected background contributions in the RPC signal regions with zero or one b-jet requirement. The "Rare" category contains the contributions from associated production of $t\bar{t}$ with $h/WW/t/t\bar{t}$, as well as tZ, tWZ, Wh, Zh, and triboson production. Background categories shown as "–" denote that they cannot contribute to a given region (charge-flip in 3-lepton regions). The displayed yields include all sources of statistical and systematic uncertainties. The individual uncertainties can be correlated and therefore do not necessarily add up in quadrature to the uncertainty on the total expected background.

	SR3L1	SR3L2	SR0b1	SR0b2	SR1b
Observed	6	2	5	0	12
Total SM background	6.1 ± 2.2	1.2 ± 0.5	8.8 ± 2.9	1.6 ± 0.8	11.4 ± 2.8
$t\bar{t}Z$	0.69 ± 0.25	0.10 ± 0.04	0.45 ± 0.18	0.10 ± 0.04	1.6 ± 0.6
$t\bar{t}W$	0.09 ± 0.04	0.02 ± 0.01	0.45 ± 0.17	0.13 ± 0.06	2.0 ± 0.7
Diboson	4.2 ± 2.0	0.7 ± 0.4	3.7 ± 1.9	0.7 ± 0.5	0.5 ± 0.4
Rare	0.8 ± 0.4	0.21 ± 0.13	0.8 ± 0.4	0.18 ± 0.12	2.7 ± 0.9
Fake/non-prompt leptons	0.29 ± 0.29	0.15 ± 0.15	2.9 ± 2.0	0.4 ± 0.5	3.3 ± 2.1
Charge-flip	–	–	0.50 ± 0.09	0.08 ± 0.03	1.43 ± 0.19

Table 5: The number of observed data events and expected background contributions in the RPC signal region with a ≥ 3 b-jets requirement, and the RPV signal regions. The "Rare" category contains the contributions from associated production of $t\bar{t}$ with $h/WW/t/t\bar{t}$, as well as tZ, tWZ, Wh, Zh, and triboson production. The displayed yields include all sources of statistical and systematic uncertainties. The individual uncertainties can be correlated and therefore do not necessarily add up in quadrature to the uncertainty on the total expected background.

	SR3b	SR1b-GG	SR1b-DD	SR3b-DD
Observed	2	2	12	4
Total SM background	1.6 ± 0.6	1.7 ± 0.5	12.0 ± 2.7	1.9 ± 0.8
$t\bar{t}Z$	0.19 ± 0.07	0.26 ± 0.08	2.8 ± 0.9	0.30 ± 0.10
$t\bar{t}W$	0.17 ± 0.06	0.33 ± 0.11	1.8 ± 0.6	0.18 ± 0.07
Diboson	< 0.1	0.08 ± 0.19	0.6 ± 0.4	< 0.1
Rare	0.89 ± 0.31	0.64 ± 0.34	2.6 ± 1.3	0.8 ± 0.4
Fake/non-prompt leptons	0.2 ± 0.5	0.21 ± 0.33	2.5 ± 1.7	0.5 ± 0.6
Charge-flip	0.14 ± 0.03	0.18 ± 0.07	1.74 ± 0.22	0.14 ± 0.03

Exclusion limits are also set on the masses of the superpartners involved in the SUSY benchmark scenarios considered in this analysis. Simplified models corresponding to a single production mode and with 100% branching ratio to a specific decay chain are used, with the masses of the SUSY particles not involved in the process set to very high values. Figure 6 shows the limits on the mass of the $\tilde{\chi}_1^0$ as a function of the $\tilde{g}$ or $\tilde{b}_1$ mass for the RPC models in Fig. 1. For these results, asymptotic formulas [78] are used to model the probability distribution of the test statistic. The new limits set by this analysis can be compared with the existing limits set by other ATLAS SUSY searches [22, 80–82].

Signal models featuring gluino pair production with a subsequent gluino decay via $\tilde{\chi}_2^0$ and light sleptons ($\tilde{g} \rightarrow q\bar{q}\tilde{\chi}_2^0 \rightarrow q\bar{q}(\ell\tilde{\ell}^*/\nu\tilde{\nu}^*) \rightarrow q\bar{q}(\ell^+\ell^-/\nu\nu)\tilde{\chi}_1^0$) are probed using SR3L1 and SR3L2 (Fig. 6(a)). In

Table 6: Signal model-independent upper limits on the number of BSM events (N_{BSM}) and the visible signal cross-section (σ_{vis}) in the nine SRs. The numbers (in parentheses) give the observed (expected under the SM hypothesis) 95% CL upper limits. Calculations are performed with pseudo-experiments. The $\pm 1\sigma$ variations on the expected limit due to the statistical and systematic uncertainties in the background prediction are also shown.

	SR3L1	SR3L2	SR0b1	SR0b2	SR1b
$N_{\mathrm{BSM}}^{\mathrm{obs}}$ ($N_{\mathrm{BSM}}^{\mathrm{exp}}$)	7.8 ($7.6^{+2.7}_{-1.7}$)	5.1 ($4.0^{+1.7}_{-0.4}$)	6.2 ($7.9^{+2.8}_{-1.9}$)	3.2 ($3.9^{+1.5}_{-0.4}$)	10.3 ($9.7^{+3.6}_{-2.3}$)
$\sigma_{\mathrm{vis}}^{\mathrm{obs}}$ [fb]	0.59	0.38	0.47	0.24	0.78

	SR3b	SR1b-GG	SR1b-DD	SR3b-DD
$N_{\mathrm{BSM}}^{\mathrm{obs}}$ ($N_{\mathrm{BSM}}^{\mathrm{exp}}$)	4.9 ($4.2^{+1.9}_{-0.4}$)	4.8 ($4.1^{+2.0}_{-0.4}$)	9.9 ($9.8^{+3.6}_{-2.3}$)	7.4 ($4.7^{+1.9}_{-0.9}$)
$\sigma_{\mathrm{vis}}^{\mathrm{obs}}$ [fb]	0.37	0.36	0.75	0.56

this simplified model, the gluinos decay into $u\bar{u}$, $d\bar{d}$, $s\bar{s}$ or $c\bar{c}$ with equal probabilities, and the six types of leptons are also produced in the $\tilde{\chi}_2^0$ decays with equal probabilities. The $\tilde{\chi}_2^0$ mass is set to $m_{\tilde{\chi}_2^0} = (m_{\tilde{g}} + m_{\tilde{\chi}_1^0})/2$, with the $\tilde{\ell}$ and $\tilde{\nu}$ masses set to $m_{\tilde{\ell},\tilde{\nu}} = (m_{\tilde{\chi}_2^0} + m_{\tilde{\chi}_1^0})/2$. For each point of the parameter space, the signal region providing the best expected limit is used. Gluino masses up to $m_{\tilde{g}} \approx 1.7$ TeV for a light $\tilde{\chi}_1^0$ and $\tilde{\chi}_1^0$ masses up to $m_{\tilde{\chi}_1^0} \approx 1.1$ TeV for gluinos with $m_{\tilde{g}} \approx 1.4$ TeV are excluded in this scenario, improving upon the limits set in Ref. [22] by up to 400 GeV in $\tilde{g}$ mass and up to 300 GeV in $\tilde{\chi}_1^0$ mass.

Similarly, models with gluino pair production followed by two-step gluino decays involving $\tilde{\chi}_1^\pm$ and $\tilde{\chi}_2^0$ ($\tilde{g} \to q\bar{q}\tilde{\chi}_1^\pm \to q\bar{q}W\tilde{\chi}_2^0 \to q\bar{q}WZ\tilde{\chi}_1^0$) are probed with SR0b1 and SR0b2 (Fig. 6(b)). In this simplified model, the gluinos decay into $u\bar{u}$, $d\bar{d}$, $s\bar{s}$ or $c\bar{c}$ with equal probabilities. The $\tilde{\chi}_1^\pm$ mass is set to $m_{\tilde{\chi}_1^\pm} = (m_{\tilde{g}} + m_{\tilde{\chi}_1^0})/2$ and the $\tilde{\chi}_2^0$ mass is set to $m_{\tilde{\chi}_2^0} = (m_{\tilde{\chi}_1^\pm} + m_{\tilde{\chi}_1^0})/2$; W and Z bosons produced in the decay chain are not necessarily on-shell. For each point of the parameter space, the signal region providing the best expected limit is used. The exclusion limits in this scenario reach $m_{\tilde{g}} \approx 1.6$ TeV (for light $\tilde{\chi}_1^0$) and $m_{\tilde{\chi}_1^0} \approx 900$ GeV (for $m_{\tilde{g}} \approx 1.3$ TeV), extending the limits set in Ref. [22, 80] by up to 200 GeV in $\tilde{g}$ mass and up to 350 GeV in $\tilde{\chi}_1^0$ mass.

Exclusion limits in a simplified model of bottom squark production with chargino-mediated $\tilde{b}_1 \to tW^-\tilde{\chi}_1^0$ decays are obtained with SR1b (Fig. 6(c)). In this model the $\tilde{\chi}_1^\pm$ mass is set to $m_{\tilde{\chi}_1^\pm} = m_{\tilde{\chi}_1^0} + 100$ GeV. The limits reach mass values of $m_{\tilde{b}_1} \approx 690$ GeV for a light $\tilde{\chi}_1^0$, while $m_{\tilde{\chi}_1^0} \lesssim 260$ GeV are also excluded for $m_{\tilde{b}_1} \approx 540$ GeV. This extends the limits set in Ref. [22] by up to 150 GeV in $\tilde{b}_1$ mass and up to 120 GeV in $\tilde{\chi}_1^0$ mass.

Finally, SR3b is used to set limits on masses in a simplified model with gluino pair production and $\tilde{g} \to t\bar{t}\tilde{\chi}_1^0$ decays via an off-shell top squark (Fig. 6(d)). In the compressed region where one or more of the produced top quarks is off-shell, for $m_t + m_W < m_{\tilde{g}} - m_{\tilde{\chi}_1^0} < 2m_t$, an isotropically-distributed $\tilde{g} \to tWb\tilde{\chi}_1^0$ decay is assumed, while for $2m_W < m_{\tilde{g}} - m_{\tilde{\chi}_1^0} < m_t + m_W$ an isotropically-distributed

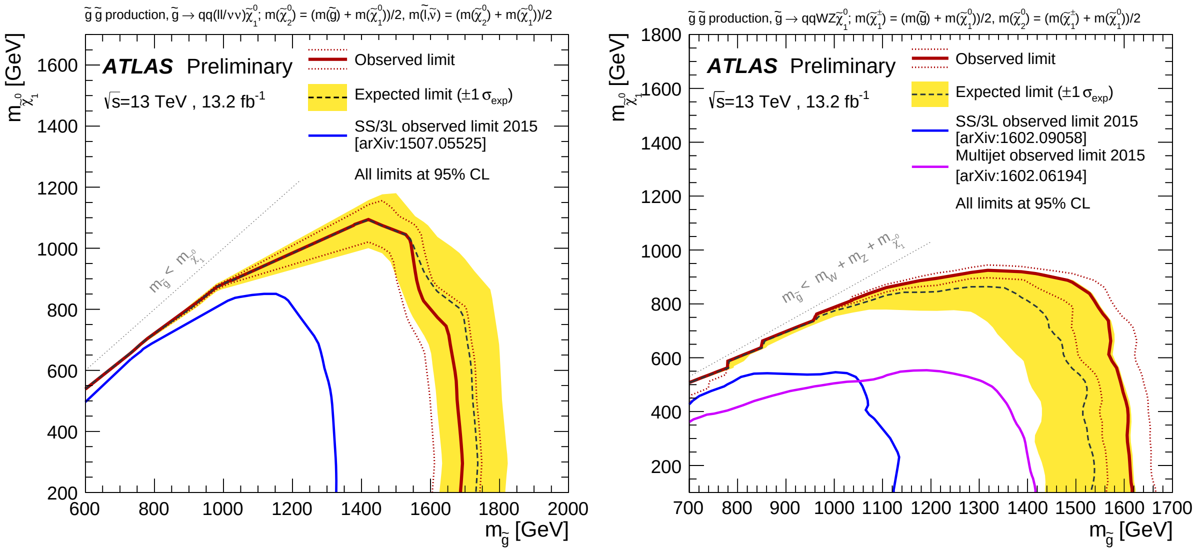

(a) SR3L1 and SR3L2, $\tilde{g} \rightarrow q\bar{q}(\ell\ell/\nu\nu)\tilde{\chi}_1^0$ scenario

(b) SR0b1 and SR0b2, $\tilde{g} \rightarrow q\bar{q}'WZ\tilde{\chi}_1^0$ scenario

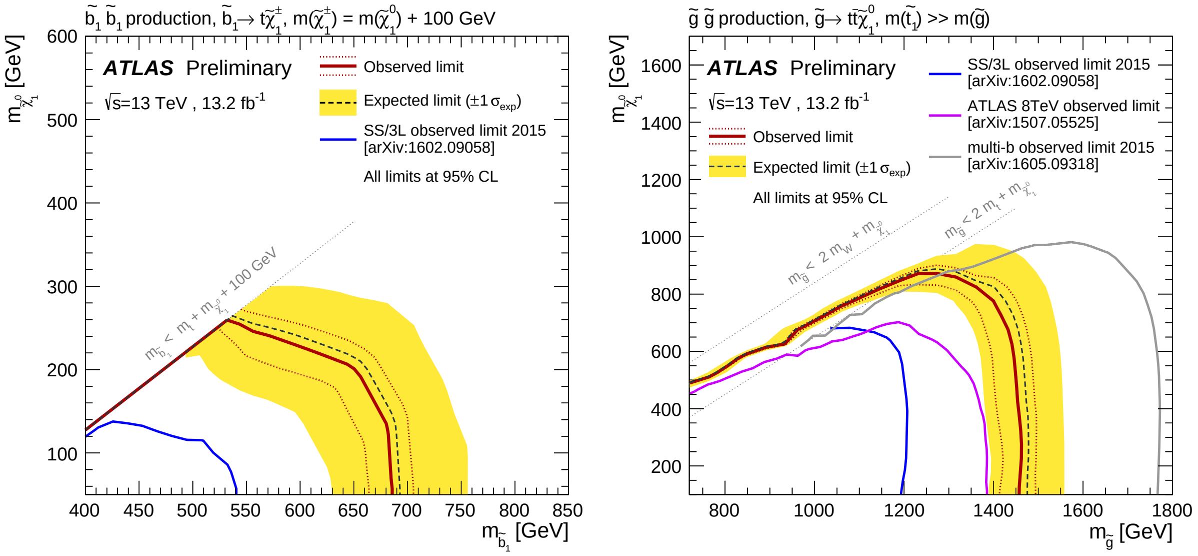

(c) SR1b, $\tilde{b}_1 \rightarrow tW^-\tilde{\chi}_1^0$ scenario

(d) SR3b, $\tilde{g} \rightarrow t\bar{t}\tilde{\chi}_1^0$ scenario

Figure 6: Observed and expected exclusion limits on the $\tilde{g}$, $\tilde{b}_1$ and $\tilde{\chi}_1^0$ masses in the context of RPC SUSY scenarios with simplified mass spectra featuring $\tilde{g}\tilde{g}$ or $\tilde{b}_1\tilde{b}_1^*$ pair production with exclusive decay modes. The signal region used to obtain the limits is specified for each scenario. The contours of the band around the expected limit are the $\pm 1\sigma$ results, including all uncertainties except theoretical uncertainties on the signal cross-section. The dotted lines around the observed limit illustrate the change in the observed limit as the nominal signal cross-section is scaled up and down by the theoretical uncertainty. All limits are computed at 95% CL. The diagonal lines indicate the kinematic limit for the decays in each specified scenario. Results are compared with the observed limits obtained by previous ATLAS searches [22, 80–82].

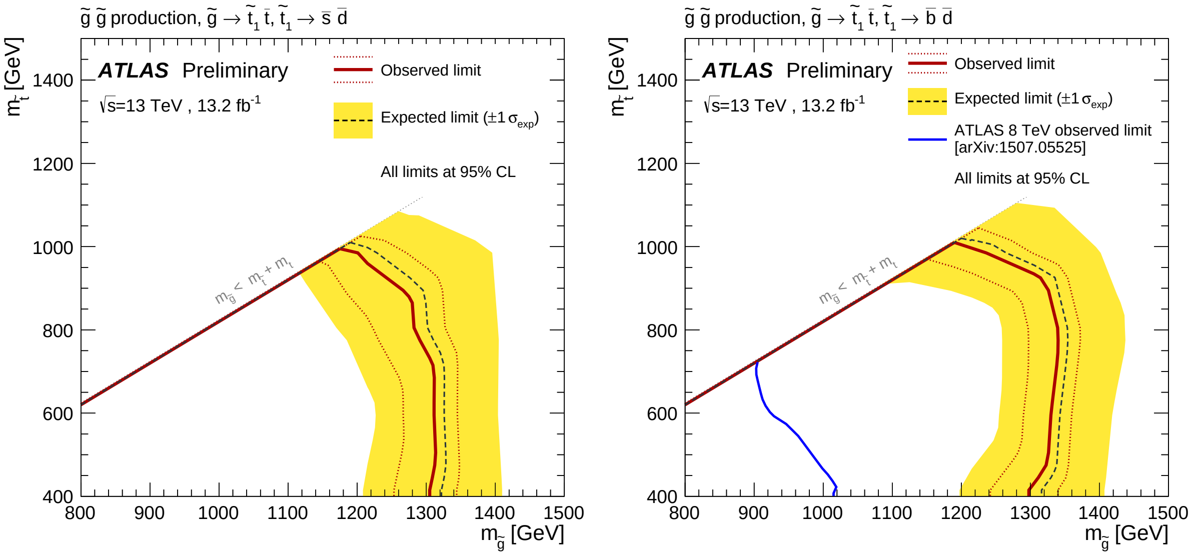

(a) SR1b-GG, $\tilde{g} \to \bar{t}\bar{s}\bar{d}$ ($\lambda''_{321} \neq 0$)

(b) SR1b-GG, $\tilde{g} \to \bar{t}\bar{b}\bar{d}$ ($\lambda''_{331} \neq 0$)

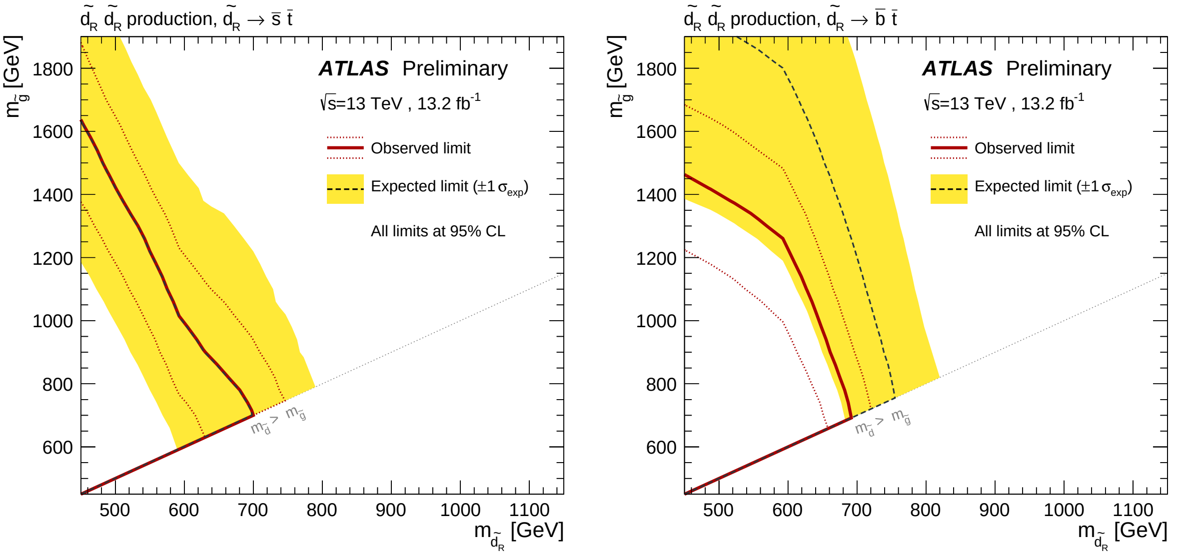

(c) SR1b-DD, $\tilde{d}_R \to \bar{t}\bar{s}$ ($\lambda''_{321} \neq 0$)

(d) SR3b-DD, $\tilde{d}_R \to \bar{t}\bar{b}$ ($\lambda''_{331} \neq 0$)

Figure 7: Observed and expected exclusion limits on the $\tilde{g}$, $\tilde{t}_1$ and $\tilde{d}_R$ masses in the context of RPV SUSY scenarios with simplified mass spectra featuring $\tilde{g}\tilde{g}$ or $\tilde{d}_R\tilde{d}_R$ pair production with exclusive decay modes. The signal region used to obtain the limits is specified for each scenario. The contours of the band around the expected limit are the $\pm 1\sigma$ results, including all uncertainties except theoretical uncertainties on the signal cross-section. The dotted lines around the observed limit illustrate the change in the observed limit as the nominal signal cross-section is scaled up and down by the theoretical uncertainty. All limits are computed at 95% CL. The diagonal lines indicate the kinematic limit for the decays in each specified scenario, or in the case of $\tilde{d}_R\tilde{d}_R$ production, the region where the alternative decay channel $\tilde{d}_R \to \tilde{g}d$ is open. Results are compared with the observed limits obtained by previous ATLAS searches [82].

$\tilde{g} \to WbWb\tilde{\chi}_1^0$ decay is used. Gluino masses of $m_{\tilde{g}} \lesssim 1.45$ TeV are excluded for $m_{\tilde{\chi}_1^0} \lesssim 700$ GeV, and $\tilde{\chi}_1^0$ masses up to $m_{\tilde{\chi}_1^0} \approx 850$ GeV are also excluded for $m_{\tilde{g}} \approx 1.25$ TeV. Limits set in Ref. [81] (dark gray line, $m_{\tilde{g}} \approx 1.75$ TeV for $m_{\tilde{\chi}_1^0} \lesssim 800$ GeV) are already beyond those reported here, but the present analysis reaches better sensitivity in the compressed region with $m_{\tilde{g}} \lesssim 2m_t + m_{\tilde{\chi}_1^0}$.

Figure 7 shows the limits on the masses of the $\tilde{g}$, $\tilde{t}_1$ and $\tilde{d}_R$ in the context of the RPV models shown in Fig. 2. For scenarios featuring gluino pair production, prompt decays of the $\tilde{t}_1$ into light SM quarks are assumed via non-zero RPV couplings λ''_{321} (for $\tilde{t}_1 \to \bar{s}\bar{d}$) or λ''_{331} (for $\tilde{t}_1 \to \bar{b}\bar{d}$). Sensitivity to these scenarios is brought by SR1b-GG, and is similar for the two $\tilde{t}_1$ decay modes, allowing to set exclusion limits up to $m_{\tilde{g}} \approx 1.3$ TeV for $m_{\tilde{t}_1} \approx 600$ TeV, or probe $m_{\tilde{t}_1}$ up to ≈ 1 TeV. These results extend the limits set in Ref. [82] by up to 400 GeV in $\tilde{g}$ mass.

Pair production of right-handed like-sign down squarks is probed by SR1b-DD and SR3b-DD, for squark decays $\tilde{d}_R \to \bar{t}\bar{s}$ or $\tilde{d}_R \to \bar{t}\bar{b}$ through respectively non-zero RPV couplings λ''_{321} or λ''_{331}. In these scenarios, simulated events are all generated with $m_{\tilde{g}} = 2$ TeV to avoid contributions beyond tree level with resonant gluinos [52, 83]; the exclusion limits are however provided as function of the $\tilde{d}_R$ and $\tilde{g}$ masses, by changing the NLO cross-section used for the normalization, which depends on the gluino mass. For $m_{\tilde{g}} \sim m_{\tilde{d}_R}$, sensitivity to $\tilde{d}_R\tilde{d}_R$ production (which does not take into account contributions from $\tilde{g}\tilde{g}$ or $\tilde{g}\tilde{q}$ production) reaches $m_{\tilde{d}_R} \approx 700$ GeV for both $\tilde{d}_R \to \bar{t}\bar{s}$ and $\tilde{d}_R \to \bar{t}\bar{b}$.

7 Conclusion

A search for supersymmetry in events with exactly two same-sign leptons or at least three leptons, multiple jets, b-jets and large $E_{\mathrm{T}}^{\mathrm{miss}}$ and/or m_{eff} is presented. The analysis is performed with proton–proton collision data at $\sqrt{s} = 13$ TeV collected between August 2015 and July 2016 with the ATLAS detector at the Large Hadron Collider corresponding to an integrated luminosity of 13.2 fb^{-1}. With no significant excess over the Standard Model expectation observed, results are interpreted in the framework of simplified models featuring gluino and squark production in R-parity conserving and R-parity violating scenarios. In the $\tilde{g}\tilde{g}$ simplified models considered, $m_{\tilde{g}} \lesssim 1.3$–$1.7$ TeV and $m_{\tilde{\chi}_1^0} \lesssim 0.85$–$1.1$ TeV are excluded at 95% confidence level depending on the model parameters. Bottom squark masses of $m_{\tilde{b}_1} \lesssim 690$ GeV are also excluded for a light $\tilde{\chi}_1^0$ in a $\tilde{b}_1\tilde{b}_1^*$ simplified model with $\tilde{b}_1 \to tW^-\tilde{\chi}_1^0$. Right-handed down squark masses are probed up to $m_{\tilde{d}_R} \approx 700$ GeV in RPV scenarios. Within the models considered, exclusion limits are extended by 150–400 GeV in $\tilde{g}$ mass, 100–350 GeV in $\tilde{\chi}_1^0$ mass and 150 GeV in $\tilde{b}_1$ mass with respect to previous results.

References

[1] Yu. A. Golfand and E. P. Likhtman,
Extension of the Algebra of Poincare Group Generators and Violation of P Invariance,
JETP Lett. **13** (1971) 323, [Pisma Zh. Eksp. Teor. Fiz.13,452(1971)].

[2] D. V. Volkov and V. P. Akulov, *Is the Neutrino a Goldstone Particle?*, Phys. Lett. **B46** (1973) 109.

[3] J. Wess and B. Zumino, *Supergauge Transformations in Four-Dimensions*,
Nucl. Phys. **B70** (1974) 39.

[4] J. Wess and B. Zumino, *Supergauge Invariant Extension of Quantum Electrodynamics*, Nucl. Phys. **B78** (1974) 1.

[5] S. Ferrara and B. Zumino, *Supergauge Invariant Yang-Mills Theories*, Nucl. Phys. **B79** (1974) 413.

[6] A. Salam and J. A. Strathdee, *Supersymmetry and Nonabelian Gauges*, Phys. Lett. **B51** (1974) 353.

[7] S. P. Martin, *A Supersymmetry primer*, (1997), [Adv. Ser. Direct. High Energy Phys.18,1(1998)], arXiv: `hep-ph/9709356`.

[8] P. Fayet, *Supersymmetry and Weak, Electromagnetic and Strong Interactions*, Phys. Lett. **B64** (1976) 159.

[9] P. Fayet, *Spontaneously Broken Supersymmetric Theories of Weak, Electromagnetic and Strong Interactions*, Phys. Lett. **B69** (1977) 489.

[10] G. R. Farrar and P. Fayet, *Phenomenology of the Production, Decay, and Detection of New Hadronic States Associated with Supersymmetry*, Phys. Lett. **B76** (1978) 575.

[11] H. Goldberg, *Constraint on the Photino Mass from Cosmology*, Phys. Rev. Lett. **50** (1983) 1419, [Erratum: Phys. Rev. Lett. **103** (2009) 099905].

[12] J. R. Ellis et al., *Supersymmetric Relics from the Big Bang*, Nucl. Phys. **B238** (1984) 453.

[13] N. Sakai, *Naturalness in Supersymmetric Guts*, Z. Phys. **C11** (1981) 153.

[14] S. Dimopoulos, S. Raby and F. Wilczek, *Supersymmetry and the Scale of Unification*, Phys. Rev. **D24** (1981) 1681.

[15] L. E. Ibanez and G. G. Ross, *Low-Energy Predictions in Supersymmetric Grand Unified Theories*, Phys. Lett. **B105** (1981) 439.

[16] S. Dimopoulos and H. Georgi, *Softly Broken Supersymmetry and SU(5)*, Nucl. Phys. **B193** (1981) 150.

[17] R. Barbieri and G. F. Giudice, *Upper Bounds on Supersymmetric Particle Masses*, Nucl. Phys. **B306** (1988) 63.

[18] B. de Carlos and J. A. Casas, *One loop analysis of the electroweak breaking in supersymmetric models and the fine tuning problem*, Phys. Lett. **B309** (1993) 320, arXiv: `hep-ph/9303291`.

[19] K. Inoue et al., *Aspects of Grand Unified Models with Softly Broken Supersymmetry*, Prog. Theor. Phys. **68** (1982) 927, [Erratum: Prog. Theor. Phys. **70** (1983) 330].

[20] J. R. Ellis and S. Rudaz, *Search for Supersymmetry in Toponium Decays*, Phys. Lett. **B128** (1983) 248.

[21] C. Borschensky et al., *Squark and gluino production cross sections in pp collisions at* $\sqrt{s}$ *= 13, 14, 33 and 100 TeV*, Eur.Phys.J. **C74** (2014) 3174, arXiv: `1407.5066 [hep-ph]`.

[22] ATLAS Collaboration, *Search for supersymmetry at* $\sqrt{s} = 13$ *TeV in final states with jets and two same-sign leptons or three leptons with the ATLAS detector*, Eur. Phys. J. **C76** (2016) 259, arXiv: `1602.09058 [hep-ex]`.

[23] ATLAS Collaboration, *The ATLAS Experiment at the CERN Large Hadron Collider*, JINST **3** (2008) S08003.

[24] CMS Collaboration, *Search for new physics in same-sign dilepton events in proton-proton collisions at sqrt(s) = 13 TeV*, (2016), arXiv: `1605.03171 [hep-ex]`.

[25] E. Nikolidakis and C. Smith, *Minimal Flavor Violation, Seesaw, and R-parity*, Phys.Rev. **D77** (2008) 015021, arXiv: `0710.3129 [hep-ph]`.

[26] C. Smith, *Minimal Flavor Violation as an alternative to R-parity*, (2008), arXiv: `0809.3152 [hep-ph]`.

[27] C. Csaki, Y. Grossman and B. Heidenreich, *MFV SUSY: A Natural Theory for R-Parity Violation*, Phys.Rev. **D85** (2012) 095009, arXiv: `1111.1239 [hep-ph]`.

[28] G. Durieux and C. Smith, *The same-sign top signature of R-parity violation*, JHEP **10** (2013) 068, arXiv: `1307.1355 [hep-ph]`.

[29] J. Berger et al., *The Same-Sign Dilepton Signature of RPV/MFV SUSY*, JHEP **04** (2013) 077, arXiv: `1302.2146 [hep-ph]`.

[30] ATLAS Collaboration, *2015 start-up trigger menu and initial performance assessment of the ATLAS trigger using Run-2 data*, ATL-DAQ-PUB-2016-001, 2016, URL: `https://cds.cern.ch/record/2136007/`.

[31] ATLAS Collaboration, *Improved luminosity determination in pp collisions at* $\sqrt{s} = 7$ *TeV using the ATLAS detector at the LHC*, Eur. Phys. J. C **73** (2013) 2518, arXiv: `1302.4393 [hep-ex]`.

[32] ATLAS Collaboration, *Luminosity determination in pp collisions at* $\sqrt{s} = 8$ *TeV using the ATLAS detector at the LHC*, to be submitted to Eur. Phys. J. C.

[33] ATLAS Collaboration, *The ATLAS Simulation Infrastructure*, Eur.Phys.J. **C70** (2010) 823, arXiv: `1005.4568 [physics.ins-det]`.

[34] S. Agostinelli et al., *GEANT4: A Simulation toolkit*, Nucl.Instrum.Meth. **A506** (2003) 250.

[35] ATLAS Collaboration, *The simulation principle and performance of the ATLAS fast calorimeter simulation FastCaloSim*, ATL-PHYS-PUB-2010-013, 2010, URL: `http://cds.cern.ch/record/1300517`.

[36] T. Gleisberg et al., *Event generation with SHERPA 1.1*, JHEP **02** (2009) 007, arXiv: `0811.4622 [hep-ph]`.

[37] ATLAS Collaboration, *Multi-Boson Simulation for 13 TeV ATLAS Analyses*, ATL-PHYS-PUB-2016-002, 2016, URL: `http://cds.cern.ch/record/2119986`.

[38] T. Gleisberg and S. Höche, *Comix, a new matrix element generator*, JHEP **12** (2008) 039, arXiv: `0808.3674 [hep-ph]`.

[39] F. Cascioli, P. Maierhofer and S. Pozzorini, *Scattering Amplitudes with Open Loops*, Phys. Rev. Lett. **108** (2012) 111601, arXiv: `1111.5206 [hep-ph]`.

[40] S. Schumann and F. Krauss, *A Parton shower algorithm based on Catani-Seymour dipole factorisation*, JHEP **03** (2008) 038, arXiv: `0709.1027 [hep-ph]`.

[41] S. Höche et al., *QCD matrix elements + parton showers: The NLO case*, JHEP **04** (2013) 027, arXiv: `1207.5030 [hep-ph]`.

[42] H.-L. Lai et al., *New parton distributions for collider physics*, Phys.Rev. **D82** (2010) 074024, arXiv: `1007.2241 [hep-ph]`.

[43] J. Alwall et al., *The automated computation of tree-level and next-to-leading order differential cross sections, and their matching to parton shower simulations*, JHEP **07** (2014) 079, arXiv: `1405.0301 [hep-ph]`.

[44] T. Sjöstrand, S. Mrenna and P. Z. Skands, *A Brief Introduction to PYTHIA 8.1*, Comput. Phys. Commun. **178** (2008) 852, arXiv: `0710.3820 [hep-ph]`.

[45] ATLAS Collaboration, *Modelling of the $t\bar{t}H$ and $t\bar{t}V$ $(V = W, Z)$ processes for $\sqrt{s} = 13$ TeV ATLAS analyses*, ATL-PHYS-PUB-2015-022, 2016, URL: `http://cds.cern.ch/record/2120826`.

[46] ATLAS Collaboration, *ATLAS Pythia8 tunes to 7 TeV data*, ATL-PHYS-PUB-2014-021, 2014, URL: `http://cds.cern.ch/record/1966419`.

[47] R. D. Ball et al., *Parton distributions with LHC data*, Nucl. Phys. **B867** (2013) 244, arXiv: `1207.1303 [hep-ph]`.

[48] G. Corcella et al., *HERWIG 6: An Event generator for hadron emission reactions with interfering gluons (including supersymmetric processes)*, JHEP **01** (2001) 010, arXiv: `hep-ph/0011363`.

[49] J. Pumplin et al., *New generation of parton distributions with uncertainties from global QCD analysis*, JHEP **07** (2002) 012, arXiv: `hep-ph/0201195`.

[50] LHC Higgs Cross Section Working Group, *Handbook of LHC Higgs Cross Sections: 2. Differential Distributions*, CERN-2012-002 (CERN, Geneva, 2012), arXiv: `1201.3084 [hep-ph]`.

[51] L. Lönnblad and S. Prestel, *Matching Tree-Level Matrix Elements with Interleaved Showers*, JHEP **03** (2012) 019, arXiv: `1109.4829 [hep-ph]`.

[52] W. Beenakker et al., *Squark and gluino production at hadron colliders*, Nucl.Phys. **B492** (1997) 51, arXiv: `hep-ph/9610490`.

[53] A. Kulesza and L. Motyka, *Threshold resummation for squark-antisquark and gluino-pair production at the LHC*, Phys.Rev.Lett. **102** (2009) 111802, arXiv: `0807.2405 [hep-ph]`.

[54] A. Kulesza and L. Motyka, *Soft gluon resummation for the production of gluino-gluino and squark-antisquark pairs at the LHC*, Phys.Rev. **D80** (2009) 095004, arXiv: `0905.4749 [hep-ph]`.

[55] W. Beenakker et al., *Soft-gluon resummation for squark and gluino hadroproduction*, JHEP **12** (2009) 041, arXiv: `0909.4418 [hep-ph]`.

[56] W. Beenakker et al., *Squark and gluino hadroproduction*, Int.J.Mod.Phys. **A26** (2011) 2637, arXiv: `1105.1110 [hep-ph]`.

[57] M. Krämer et al., *Supersymmetry production cross sections in pp collisions at $\sqrt{s} = 7$ TeV*, (2012), arXiv: `1206.2892 [hep-ph]`.

[58] W. Beenakker, R. Hopker and M. Spira, *PROSPINO: A Program for the production of supersymmetric particles in next-to-leading order QCD*, (1996), arXiv: `hep-ph/9611232 [hep-ph]`.

[59] D. J. Lange, *The EvtGen particle decay simulation package*, Nucl. Instrum. Meth. **A462** (2001) 152.

[60] ATLAS Collaboration, *Summary of ATLAS Pythia 8 tunes*, ATLAS-PHYS-PUB-2012-003, 2012, URL: http://cdsweb.cern.ch/record/1474107.

[61] A. D. Martin et al., *Parton distributions for the LHC*, Eur. Phys. J. **C63** (2009) 189, arXiv: 0901.0002 [hep-ph].

[62] ATLAS Collaboration, *Vertex Reconstruction Performance of the ATLAS Detector at* $\sqrt{s}$ = 13 *TeV*, ATL-PHYS-PUB-2015-026, 2015, URL: http://cdsweb.cern.ch/record/2037717.

[63] ATLAS Collaboration, *Electron efficiency measurements with the ATLAS detector using the 2015 LHC proton-proton collision data*, ATLAS-CONF-2016-024, 2016, URL: http://cds.cern.ch/record/2157687.

[64] ATLAS Collaboration, *Muon reconstruction performance of the ATLAS detector in proton–proton collision data at* $\sqrt{s}$ *=13 TeV*, Eur. Phys. J. **C76** (2016) 292, arXiv: 1603.05598 [hep-ex].

[65] M. Cacciari, G. P. Salam and G. Soyez, *The anti-kt jet clustering algorithm*, JHEP **04** (2008) 063, arXiv: 0802.1189 [hep-ph].

[66] ATLAS Collaboration, *Topological cell clustering in the ATLAS calorimeters and its performance in LHC Run 1*, (2016), arXiv: 1603.02934 [hep-ex].

[67] ATLAS Collaboration, *Jet Calibration and Systematic Uncertainties for Jets Reconstructed in the ATLAS Detector at* $\sqrt{s}$ = 13 *TeV*, ATL-PHYS-PUB-2015-015, 2015, URL: http://cds.cern.ch/record/2028594.

[68] ATLAS Collaboration, *Tagging and suppression of pileup jets with the ATLAS detector*, ATLAS-CONF-2014-018, 2014, URL: http://cdsweb.cern.ch/record/1700870.

[69] ATLAS Collaboration, *Performance of b-Jet Identification in the ATLAS Experiment*, JINST **11** (2016) P04008, arXiv: 1512.01094 [hep-ex].

[70] ATLAS Collaboration, *Expected performance of the ATLAS b-tagging algorithms in Run-2*, ATL-PHYS-PUB-2015-022, 2015, URL: http://cds.cern.ch/record/2037697.

[71] ATLAS Collaboration, *Optimisation of the ATLAS b-tagging performance for the 2016 LHC Run*, ATL-PHYS-PUB-2016-012, 2016, URL: http://cds.cern.ch/record/2160731.

[72] ATLAS Collaboration, *Measurements of the photon identification efficiency with the ATLAS detector using* 4.9 fb^{-1} *of pp collision data collected in 2011*, ATLAS-CONF-2012-123, 2012, URL: http://cdsweb.cern.ch/record/1473426.

[73] ATLAS Collaboration, *Performance of missing transverse momentum reconstruction for the ATLAS detector in the first proton-proton collisions at at* $\sqrt{s}$*= 13 TeV*, ATL-PHYS-PUB-2015-027, 2015, URL: http://cds.cern.ch/record/2037904.

[74] ATLAS Collaboration, *Expected performance of missing transverse momentum reconstruction for the ATLAS detector at* $\sqrt{s}$ *= 13 TeV*, ATL-PHYS-PUB-2015-023, 2015, URL: http://cds.cern.ch/record/2037700.

[75] ATLAS Collaboration, *Data-Quality Requirements and Event Cleaning for Jets and Missing Transverse Energy Reconstruction with the ATLAS Detector in Proton–Proton Collisions at a Center-of-Mass Energy of* $\sqrt{s}$ = 7 *TeV*, ATLAS-CONF-2010-038, 2010, URL: http://cdsweb.cern.ch/record/1277678.

[76] ATLAS Collaboration,
Search for supersymmetry using events with three leptons, multiple jets, and missing transverse momentum in 13.0 *fb^{-1} of pp collisions with the ATLAS detector at* $\sqrt{s} = 8$ *TeV*, ATLAS-CONF-2012-151, 2012, URL: `http://cdsweb.cern.ch/record/1493490`.

[77] M. Baak et al., *HistFitter software framework for statistical data analysis*, Eur. Phys. J. **C75** (2015) 153, arXiv: `1410.1280 [hep-ex]`.

[78] G. Cowan et al., *Asymptotic formulae for likelihood-based tests of new physics*, Eur. Phys. J. **C71** (2011) 1554, [Erratum: Eur. Phys. J. **C73** (2013) 2501], arXiv: `1007.1727 [physics.data-an]`.

[79] A. L. Read, *Presentation of search results: the CL s technique*, Journal of Physics G: Nuclear and Particle Physics **28** (2002) 2693.

[80] ATLAS Collaboration, *Search for new phenomena in final states with large jet multiplicities and missing transverse momentum with ATLAS using* $\sqrt{s}$ *= 13 TeV proton-proton collisions*, Phys. Lett. **B757** (2016) 334, arXiv: `1602.06194 [hep-ex]`.

[81] ATLAS Collaboration,
Search for pair production of gluinos decaying via stop and sbottom in events with b-jets and large missing transverse momentum in pp collisions at $\sqrt{s} = 13$ *TeV with the ATLAS detector*, (2016), arXiv: `1605.09318 [hep-ex]`.

[82] ATLAS Collaboration, *Summary of the searches for squarks and gluinos using* $\sqrt{s} = 8$ *TeV pp collisions with the ATLAS experiment at the LHC*, JHEP **10** (2015) 054, arXiv: `1507.05525 [hep-ex]`.

[83] D. Gonçalves-Netto et al., *Automated Squark and Gluino Production to Next-to-Leading Order*, Phys. Rev. **D87** (2013) 014002, arXiv: `1211.0286 [hep-ph]`.

Appendix

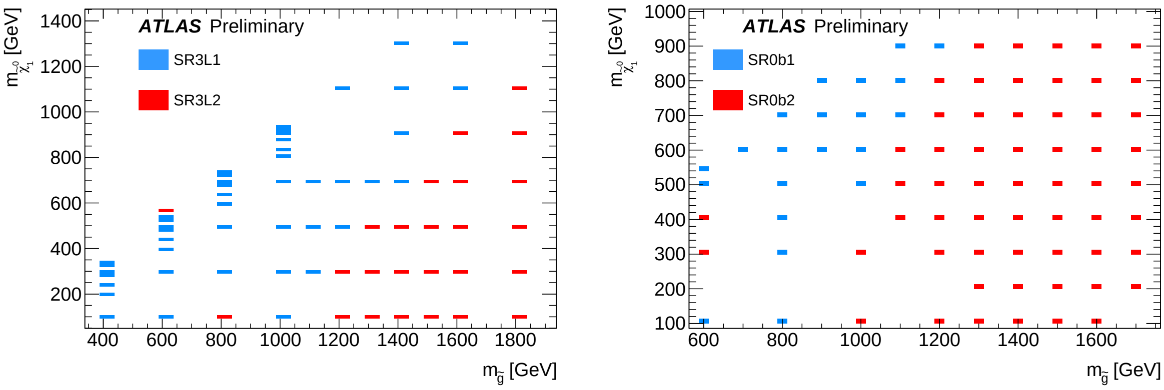

Figure 8: Illustration of the best expected signal region per signal grid point for the $\tilde{g} \rightarrow q\bar{q}(\ell\ell/\nu\nu)\tilde{\chi}_1^0$ (left) and $\tilde{g} \rightarrow q\bar{q}'WZ\tilde{\chi}_1^0$ (right) models. This mapping is used for the final combined exclusion limits.

Table 7: Number of signal events selected at different stages of the SR3L1, SR3L2, SR0b1 and SR0b2 definitions, for some of the RPC benchmark scenarios shown on Fig. 1. Only the statistical uncertainties are displayed.

	Raw events	Number of events expected for $L = 13.2$ fb^{-1}
SR3L1, $\tilde{g} \to q\bar{q}(\ell\ell/\nu\nu)\tilde{\chi}_1^0$, $m_{\tilde{g}} = 1.4$ TeV, $m_{\tilde{\chi}_1^0} = 1.1$ TeV		
produced	21016	304
≥ 3 leptons ($p_T > 20, 20, 10$ GeV)	2084	28.8 ± 0.8
trigger	2071	28.5 ± 0.8
no b-jet ($p_T > 20$ GeV)	1849	25.5 ± 0.8
≥ 4 jets ($p_T > 40$ GeV)	841	11.5 ± 0.5
$E_T^{miss} > 150$ GeV	553	7.5 ± 0.4
SR3L2, $\tilde{g} \to q\bar{q}(\ell\ell/\nu\nu)\tilde{\chi}_1^0$, $m_{\tilde{g}} = 1.8$ TeV, $m_{\tilde{\chi}_1^0} = 300$ GeV		
produced	19395	33
≥ 3 leptons ($p_T > 20, 20, 10$ GeV)	2566	4.23 ± 0.11
trigger	2562	4.22 ± 0.11
no b-jet ($p_T > 20$ GeV)	2138	3.50 ± 0.10
≥ 4 jets ($p_T > 40$ GeV)	1933	3.18 ± 0.09
$E_T^{miss} > 200$ GeV	1624	2.70 ± 0.09
$m_{eff} > 1.5$ TeV	1622	2.69 ± 0.09
SR0b1, $\tilde{g} \to q\bar{q}'WZ\tilde{\chi}_1^0$, $m_{\tilde{g}} = 1.1$ TeV, $m_{\tilde{\chi}_1^0} = 800$ GeV		
produced	20000	2158
≥ 2 SS leptons ($p_T > 20$ GeV)	515	54.3 ± 3.1
trigger	478	49.7 ± 3.0
no b-jet ($p_T > 20$ GeV)	358	35.6 ± 2.4
≥ 6 jets ($p_T > 25$ GeV)	206	21.3 ± 1.9
$E_T^{miss} > 150$ GeV	112	11.7 ± 1.4
$m_{eff} > 500$ GeV	112	11.7 ± 1.4
SR0b2, $\tilde{g} \to q\bar{q}WZ\tilde{\chi}_1^0$, $m_{\tilde{g}} = 1.6$ TeV, $m_{\tilde{\chi}_1^0} = 400$ GeV		
produced	20000	107
≥ 2 SS leptons ($p_T > 20$ GeV)	1021	5.20 ± 0.21
trigger	1005	5.07 ± 0.20
no b-jet ($p_T > 20$ GeV)	693	3.54 ± 0.17
≥ 6 jets ($p_T > 40$ GeV)	559	2.77 ± 0.15
$E_T^{miss} > 150$ GeV	505	2.54 ± 0.14
$m_{eff} > 900$ GeV	505	2.54 ± 0.14

Table 8: Number of signal events selected at different stages of the SR1b and SR3b definitions, for some of the RPC benchmark scenarios shown on Fig. 1. Only the statistical uncertainties are displayed.

SR1b, $\tilde{b}_1 \to t\tilde{\chi}_1^{\pm}$, $m_{\tilde{b}_1} = 700\,\text{GeV}$, $m_{\tilde{\chi}_1^{\pm}} = 150\,\text{GeV}$, $m_{\tilde{\chi}_1^0} = 50\,\text{GeV}$		
produced	94082	885
≥ 2 SS leptons ($p_T > 20\,\text{GeV}$)	5191	46.9 ± 0.8
trigger	4913	43.7 ± 0.8
≥ 1 b-jet ($p_T > 20\,\text{GeV}$)	4239	37.5 ± 0.7
≥ 6 jets ($p_T > 25\,\text{GeV}$)	2034	18.2 ± 0.5
$E_T^{\text{miss}} > 200\,\text{GeV}$	1060	9.6 ± 0.4
$m_{\text{eff}} > 650\,\text{GeV}$	1060	9.6 ± 0.4

SR3b, $\tilde{g} \to t\bar{t}\tilde{\chi}_1^0$, $m_{\tilde{g}} = 1.3\,\text{TeV}$, $m_{\tilde{\chi}_1^0} = 945\,\text{GeV}$		
produced	96000	607
≥ 2 SS leptons ($p_T > 20\,\text{GeV}$)	3612	21.0 ± 0.4
trigger	3332	19.0 ± 0.4
≥ 3 b-jets ($p_T > 20\,\text{GeV}$)	1495	8.87 ± 0.30
≥ 6 jets ($p_T > 25\,\text{GeV}$)	1150	6.80 ± 0.26
$E_T^{\text{miss}} > 150\,\text{GeV}$	514	3.11 ± 0.18
$m_{\text{eff}} > 600\,\text{GeV}$	511	3.08 ± 0.18

Table 9: Number of signal events selected at different stages of the SR1b-GG, SR1b-DD and SR3b-DD definitions, for some of the RPV benchmark scenarios shown on Fig. 2. Only the statistical uncertainties are displayed.

SR1b-GG, $\tilde{g} \to tds$, $m_{\tilde{g}} = 1.4\,\text{TeV}$, $m_{\tilde{t}_1} = 600\,\text{GeV}$		
produced	20000	334
≥ 2 SS leptons ($p_T > 20\,\text{GeV}$)	279	4.20 ± 0.32
trigger	261	3.83 ± 0.30
≥ 1 b-jet ($p_T > 20\,\text{GeV}$)	227	3.24 ± 0.27
≥ 6 jets ($p_T > 50\,\text{GeV}$)	194	2.78 ± 0.25
$m_{\text{eff}} > 1.8\,\text{TeV}$	188	2.71 ± 0.25

SR1b-DD, $\tilde{d}_R \to \bar{t}\bar{s}$, $m_{\tilde{d}_R} = 600\,\text{GeV}$, $m_{\tilde{g}} = 1.2\,\text{TeV}$		
produced	20000	1005
≥ 2 leptons ($q < 0$, $p_T > 20\,\text{GeV}$)	454	21.9 ± 1.3
trigger	414	19.2 ± 1.2
≥ 1 b-jet ($p_T > 20\,\text{GeV}$)	359	16.8 ± 1.1
≥ 4 jets ($p_T > 50\,\text{GeV}$)	259	11.9 ± 0.9
$m_{\text{eff}} > 1.2\,\text{TeV}$	169	8.2 ± 0.8

SR3b-DD, $\tilde{d}_R \to \bar{t}\bar{b}$, $m_{\tilde{d}_R} = 600\,\text{GeV}$, $m_{\tilde{g}} = 1.2\,\text{TeV}$		
produced	20000	1005
≥ 2 leptons ($q < 0$, $p_T > 20\,\text{GeV}$)	508	24.6 ± 1.4
trigger	469	22.1 ± 1.3
≥ 3 b-jets ($p_T > 20\,\text{GeV}$)	242	11.4 ± 0.9
≥ 4 jets ($p_T > 50\,\text{GeV}$)	185	8.7 ± 0.8
$m_{\text{eff}} > 1\,\text{TeV}$	159	7.6 ± 0.8